

UCLA

UCLA Electronic Theses and Dissertations

Title

Theoretical Studies on Organic Catalysis: N-Heterocyclic Carbene Catalyzed Ring-Opening Polymerization and Initiation of Z-selective Olefin Metathesis with Ruthenium Catalysts

Permalink

<https://escholarship.org/uc/item/2qw44013>

Author

Dong, Xiaofei

Publication Date

2016

Peer reviewed|Thesis/dissertation

UNIVERSITY OF CALIFORNIA

Los Angeles

Theoretical Studies on Organic Catalysis:
N-Heterocyclic Carbene Catalyzed Ring-Opening Polymerization
and Initiation of Z-selective Olefin Metathesis
with Ruthenium Catalysts

A thesis submitted in partial satisfaction of the
requirements for the degree of Master of Science
in Chemistry

by

Xiaofei Dong

2016

© Copyright by

Xiaofei Dong

2016

ABSTRACT OF THE THESIS

Theoretical Studies on Organic Catalysis:
N-Heterocyclic Carbene Catalyzed Ring-Opening Polymerization
and Initiation of Z-selective Olefin Metathesis
with Ruthenium Catalysts

by

Xiaofei Dong

Master of Science in Chemistry

University of California, Los Angeles, 2016

Professor Kendall N. Houk, Chair

The mechanism of NHC catalyzed ring-opening polymerization of lactide and the factors controlling the reactivities of photoswitchable NHC catalysts have been investigated with the DFT method. The general base mechanism is favored comparing to the nucleophilic mechanism for the ring-opening polymerization of lactide catalyzed by NHC. The reactivities of the NHC catalysts are determined by their electrophilicities. The NHCs which are highly electrophilic form adducts

in the presence of alcohol. These mechanistic studies will help the design of novel multifunctional catalysts.

The initiation mechanism of *Z*-selective ruthenium catalysts and the effects of anionic ligands on the initiation rates are studied with DFT calculation. The dissociative pathway is favored for the initiation and the metallacyclobutane cycloreversion is the rate determining step. Catalysts with more steric bulk and less nucleophilic ligands have higher initiation rates because of the structural differences between the precatalyst and the transition state.

The thesis of Xiaofei Dong is approved.

Miguel A. Garcia-Garibay

Neil Kamal Garg

Kendall N. Houk, Committee Chair

University of California, Los Angeles

2016

Acknowledgements and Dedication

I would like to express my deep gratitude to my advisor Professor Kendall N. Houk for his generous and strong support during my graduate research. I would like to thank all the professors in the organic division as well for their help and understanding during my study at UCLA. I am grateful for the assistance given by Dr. Peng Liu during my early years of graduate study and his help with the research on organometallic catalysts. I would also like to thank Dr. Yanwei Li for his collaboration and helpful discussions on the lactide polymerization studies.

My special thanks are given to our collaborators, Prof. Grubbs at Caltech and Prof. Bielawski at UNIST. I would also like to thank Prof. Truhlar at University of Minnesota for his kind explanations about solvation models through email.

Finally, I wish to thank my parents for their support and encouragement throughout my study.

Table of Contents

ABSTRACT OF THE THESIS	ii
Acknowledgements and Dedication	v
Table of Contents	vi
List of Figures	ix
List of Tables	xii
List of Schemes	xiii
I. General Introduction	1
II. Computational Methods	3
2.1 Density Functional Theory (DFT)	3
2.2 Basis Sets	5
2.3 Solvation Model	6
2.4 Intrinsic Reaction Coordinate (IRC) Calculation	7
2.5 Programs and Facilities	8
III. Lactide Ring-Opening Polymerization Catalyzed with the N-Heterocyclic Carbene Catalyst	9
3.1 Introduction	9
3.1.1. Introduction of Polylactides and Polyglycolides	9
3.1.2. Metallic Catalysts for Ring-Opening Polymerization of Lactide and Glycolide ..	10
3.1.3. Stereocontrolled Ring-opening Polymerization with Metallic Catalysts	10
3.1.4. Organocatalysts for Ring-Opening Polymerization of Lactide and Glycolide	13
3.1.5. N-Heterocyclic Carbene Catalysts	15
3.1.5.1. General Introduction	15
3.1.5.2. Photoswitchable NHC Catalyst	16
3.1.5.3. Stereocontrol of NHC catalyst in ROP of Lactide	18
3.1.5.4. Mechanistic Studies with NHC Catalyzed Ring-Opening Reactions	18
3.2 Computational Details	22
3.3 Results and Discussion	23
3.3.1 NHC-catalyzed Glycolide Polymerization	23

3.3.1.1	General Base Pathway and Nucleophilic Pathway	23
3.3.1.2	Detailed Discussion on the Energy Profile	27
3.3.2	NHC-catalyzed Lactide Polymerization	32
3.3.3	Theoretical Study on the Photoswitchable NHC Catalysts	34
3.3.4	Solvation Model Comparison	38
3.4	Conclusion	42
IV.	Initiation with Z-Selective Ruthenium Catalysts – Mechanism and Anionic Effects	43
4.1	Introduction	43
4.1.1	Olefin Metathesis	43
4.1.1.1	Background	43
4.1.1.2	Ruthenium Catalysts for Olefin Metathesis	45
4.1.2	Z-Selective Olefin Metathesis	47
4.1.2.1	Molybdenum and Tungsten Z-Selective Catalysts	48
4.1.2.2	Ruthenium Z-Selective Catalysts	49
4.1.3	Initiation Mechanism with Ruthenium Olefin Metathesis Catalysts	53
4.1.3.1	Initiation Mechanism of the Second Generation of Grubbs Catalysts	53
4.1.3.2	Initiation Studies on Z-Selective Ruthenium Catalysts	54
4.2	Computational Details	57
4.3	Results and Discussion	58
4.3.1	Initiation Mechanism of Z-selective Ruthenium Catalysts	58
4.3.1.1	Dissociative Mechanism	59
4.3.1.1.1	Dissociation of the Ligand	59
4.3.1.1.2	Bottom-bound vs. Side-bound Metathesis	61
4.3.1.2	Associative Mechanism	65
4.3.1.2.1	Association of the Olefin Substrate	66
4.3.1.2.2	Metathesis Pathway for Initiation by the Association Mechanism	67
4.3.1.3	Summary and the Free Energy Profile	70
4.3.2	Anionic Effects with Initiation Process	72
4.3.2.1	Steric Effects of the Anionic Ligands	72

4.3.2.2 Electronic Effects of the Anionic Ligands	74
4.3.2.3 Initiation Mechanism of the Monodentate Ruthenium Catalysts	76
4.3.2.4 Summary of Anionic Effects	79
4.4 Conclusion	81
References	82

List of Figures

Figure III-1 Structures of glycolide and lactide isomers.	9
Figure III-2 Stereoselective catalysts with chiral ligands.	12
Figure III-3 Stereoselective aluminum catalyst with achiral ligands.	13
Figure III-4 Typical organocatalysts for ROP of cyclic esters.	14
Figure III-5 Reaction pathways and free energies (kcal/mol) for the 1,3,4,5-tetramethylimidazol-2-ylidene catalyzed ring opening of caprolactone in the presence of methanol by the nucleophilic (red) and hydrogen-bonding (blue) mechanisms.	20
Figure III-6 Energy profile of general base pathway (blue) and nucleophilic pathway (green) for IMes catalyzed glycolide polymerization in the presence of methanol.	25
Figure III-7 Optimized structures in the general base pathway.	27
Figure III-8 Optimized structure of glycolide is in boat conformation.	28
Figure III-9 Transition state conformation of the nucleophilic attack by alcohol.	28
Figure III-10 Optimized structures in the nucleophilic pathway.	30
Figure III-11 Optimized structures and free energies of the transition states of the rate-determining step in lactide polymerization.	32
Figure III-12 Anti attack with respect to the methyl group.	33
Figure IV-1 One of Schrock's molybdenum catalysts.	44
Figure IV-2 The first generation of Grubbs catalyst (G1).	45
Figure IV-3 The second generation of Grubbs catalyst (G2).	45
Figure IV-4 Hoveyda-Grubbs catalyst (GH2).	46
Figure IV-5 Molybdenum or tungsten based MAP Z-selective catalysts.	48
Figure IV-6 Synthesis of ruthenium Z-selective catalyst.	49

Figure IV-7 Bottom-bound pathway is favored for Grubbs II catalysts.....	50
Figure IV-8 Side-bound pathway is favored for chelated Ru catalysts with DFT calculation....	50
Figure IV-9 Energy and optimized structures of transition states in Z-selective and E-selective pathways.	51
Figure IV-10 Grubbs II catalysts undergoes dissociation mechanism for catalyst initiation.	53
Figure IV-11 Dissociation of ligand through bond rotation.	59
Figure IV-12 Transition states of ortho-isopropoxy group rotation in the dissociative mechanism.	60
Figure IV-13 Structure isomer of precatalyst 30	60
Figure IV-14 The five-coordinated complex is formed after alkylidene-aryl C-C bond rotation.	61
Figure IV-15 Optimized structure of TS2b-Dis	63
Figure IV-16 The monodentate and bidentate structures of TS2s-Dis	64
Figure IV-17 Side view of the bidentate structure of TS2S-Dis	65
Figure IV-18 Optimized structure of CPL1s-Ass	66
Figure IV-19 Optimized structures of transition states in the associative mechanism.	68
Figure IV-20 Optimized structure of TS2b-Ass	69
Figure IV-21 Energy profile of the initiation mechanism of the Z-selective Ru catalyst.	70
Figure IV-22 The transition state structures of metallacyclobutane cycloreversion of 27 and 26	72
Figure IV-23 Steric repulsions exist in the precatalyst 26	73
Figure IV-24 Optimized structure of 29	75
Figure IV-25 Optimized transition state structure of the metallacyclobutane cycloreversion.	75

Figure IV-26 Optimized structure of 31	76
Figure IV-27 Rate determining transition state structures of the four possible initiation pathways of 31	77
Figure IV-28 The first step in the dissociative initiation of 31	78
Figure IV-29 Metathesis steps in the initiation of 31	78
Figure IV-30 Correlation of experimental rate constant and computational free energy barrier of chelated Ru catalysts with different anionic ligands.....	80
Figure IV-31 Correlation of experimental rate constant and computational free energy barrier of chelated Ru catalysts with different anionic ligands (excluding nitrate ligated catalyst).....	80

List of Tables

Table III-1 Relative free energies of NHC alcohol adducts.	36
Table III-2 Free energies in NHC catalyzed ROP of glycolide by CPCM and SMD solvation model.....	38
Table III-3 Entropies in NHC catalyzed ROP of glycolide by CPCM and SMD solvation model.	39
Table III-4 Free energies calculated with different N-substituents.	40
Table IV-1 Initiation rate constants with various ruthenium catalysts.	55
Table IV-2 The experimental initiation rates and computational activation barriers with different anionic ligands.	79

List of Schemes

Scheme III-1	General mechanism of metal catalyzed ring-opening polymerization of lactide. 10
Scheme III-2	Tacticity of polylactides from different monomers. 11
Scheme III-3	Photoswitchable NHC catalyst for ROP of ϵ -caprolactone. 16
Scheme III-4	Proposed catalytic cycle for a photoswitchable NHC-catalyzed ringopening polymerization. 17
Scheme III-5	Photoswitchable NHC catalyst for lactide polymerization. 17
Scheme III-6	General base pathway and nucleophilic pathway. 23
Scheme III-7	Free energies of the open and closed form of the photoswitchable catalyst and their alcohol adducts. 34
Scheme IV-1	Olefin metathesis reaction. 43
Scheme IV-2	A four-member ring intermediate is formed during olefin metathesis according to Chauvin's mechanism. 43
Scheme IV-3	Synthesis of insect pheromones with olefin metathesis. 47
Scheme IV-4	Dissociative and associative mechanism. 58
Scheme IV-5	The bottom-bound pathway in the dissociative mechanism. 62
Scheme IV-6	The side-bound pathway in the dissociative mechanism. 63
Scheme IV-7	Association of the Olefin Substrate from the side position. 66
Scheme IV-8	The side-bound pathway in the associative mechanism. 67
Scheme IV-9	The bottom-bound pathway in the associative mechanism. 69

I. General Introduction

Catalysts have been playing important roles in organic reactions for centuries. Both the organocatalysts and organometallic catalysts are applied in organic synthesis today. These catalysts promote reactions by changing the reaction pathways and lowering the free energy barriers of the reactions. Understanding the mechanisms of catalytic processes contributes to the development of high-efficiency catalysts and the design of catalysts with new functions.

Computational chemistry, a rapidly growing field in the last decades, has been widely applied to the study of organic catalysts. With the computational theories such as quantum mechanics and molecular mechanics, the geometries and energies of intermediates produced in chemical reactions are calculated and the transition state structures are located. By comparing the energies of the transition states and intermediates in different pathways, the most favorable pathways are identified and the energy barriers of the reactions are calculated. Detailed catalytic mechanisms are determined and catalyst designs can be made based on the reaction mechanism and the geometries of the catalysts and substrates during the reaction pathway.

In this thesis, both the organic reactions catalyzed with organocatalysts and those catalyzed with organometallic catalysts have been explored with computational methods.

Chapter II briefly summarizes the typical computational methods and facilities used in this thesis. Some basic concepts about computational chemistry are introduced.

Chapter III introduces the mechanistic investigation of the ring-opening polymerization of lactones, especially lactide. The catalysts studied in this chapter are the N-heterocyclic carbene (NHC) catalysts, which are among the most versatile organic catalysts. The general-base mechanism and the nucleophilic mechanism of the NHC catalyzed ring-opening polymerizations

are compared with computational studies. Designed photoswitchable NHC catalysts are also studied.

Chapter IV reports the investigation of the initiation mechanism of olefin metathesis catalyzed with the chelated ruthenium catalysts. The initiation process of the catalytic reaction, in which the precatalyst is converted to the active catalyst involved in the olefin metathesis reaction, is investigated. Catalysts with different anionic ligands are compared mechanistically.

II. Computational Methods

2.1 DENSITY FUNCTIONAL THEORY (DFT)

Density functional theory (DFT) is a form of quantum mechanics that is one of the most popular computational method in chemistry nowadays. It gives accurate results at relative low cost of computational resources. Current DFT methods are based on the two theorems which were published by Hohenberg and Kohn in 1964,¹ and Kohn and Sham in 1965.² According to the theorems, the energy of a molecule and all other properties can be determined from its electron density. Kohn and Sham also showed how to derive electron densities from orbitals of non-interacting electrons, the so-called Kohn-Sham orbitals. The energy of the molecule can be expressed as a functional of the electron density. The electron density, ρ , is a function of the three position variables:

$$E_0 = F[\rho(x, y, z)] \quad (2-1)$$

E_0 is the energy of the molecule at ground state and ρ is the electron density which is the function of (x, y, z) . F is the functional that gives the energy.

If we knew the accurate electron density and the correct energy functional, we could obtain the true energy of the molecule. In fact, the exact energy functional is unknown, so DFT calculations use approximate functionals, and ongoing research seeks more accurate functionals.

The energy of a molecule includes the electronic kinetic energies, the nucleus-electron attraction potential energies, the electron-electron repulsion potential energies and the exchange-correlation energy:

$$E(\rho) = T(\rho) + V_{nc}(\rho) + J_{ee}(\rho) + E_{xc}(\rho) \quad (2-2)$$

E is the energy of the molecule, T is the electronic kinetic energy, V_{ne} is the potential attraction between nuclei and electrons, J_{ee} is the electronic repulsions and E_{xc} is the exchange-correlation energy.

While the first three terms of the functional are well-known, nature of the exchange-correlation term is not known analytically. Different DFT methods use different exchange-correlation functionals, and they are derived often from parameterization and comparisons to empirical data.

The most commonly used DFT methods today are the B3LYP method for molecules, and the PBE method for materials. B3LYP contains a hybrid exchange functional with three parameters developed by Becke³ and a correlation functional by Lee, Yang and Parr.⁴ In this method, the exchange functional is hybridized with the Hartree-Fock exchange functional so the accuracy of this method is good in many cases, especially for the geometry optimization and frequency calculation of metal and non-metal systems.

The weakness of the B3LYP method is that it does not consider the factors influencing the long-range interactions of molecules. London dispersion interactions are important in many cases and cannot be neglected. One of the solutions to this deficiency is the dispersion correction proposed by Stefan Grimme.⁵ The most recent and commonly used version is the D3 method developed in 2010.⁶ It is based on an atom pairwise additive treatment of the dispersion energy:

$$E_{\text{DFT-D}} = E_{\text{KS-DFT}} + E_{\text{disp}} \quad (2-3)$$

Another method to address the problem is the utility of Minnesota functionals developed by Truhlar.⁷ These functionals are based on the meta-hybrid GGA and meta-GGA functionals. The highly parameterized meta-GGAs incorporate kinetic energy density quantitatively and seem to account for dispersion effects.⁸ The M06 functional is the one which has been widely used in single

point energy calculations for main group and transition metal calculations. It is a global hybrid functional with 27% Hartree-Fock exchange.

2.2 BASIS SETS

A basis set is a set of functions to describe the atomic orbitals, and that are combined to describe molecular orbitals. Choosing the proper basis set is as important as using the appropriate method in DFT calculation. The most basic way to describe the molecular orbitals is with Slater-type orbitals (STOs) that resemble the hydrogenic orbitals obtained as solutions to the Schrodinger equation. STOs accurately describe atomic orbitals with the function in which the electron density decays exponentially with the distance from the nuclei (e^{-r}). However, the integral calculations of the Slater-type orbitals are difficult, and consequently, Gaussian-type orbitals (GTOs) are used instead in computation.⁹ These functions have the form of e^{-r^2} .

The linear combination of Gaussian-type orbitals is used to mimic the Slater-type orbitals in most calculations. In a minimal basis set, there is one basis function for each occupied orbital in the atom and the minimal basis set is referred to as single-zeta (SZ) basis set. Zeta is the Greek letter that is a scaling factor in the exponent. If two basis functions are used to describe each orbital of the atom, it is referred to as double-zeta (DZ).

In the basis set 6-31G(d), the dash separates the number of functions used to describe the inner shell from those used to describe the valence shell. The “6” on the left of the dash represents the core basis function consists of a linear combination of six Gaussian functions. The two digits on the right of the dash tells that the valence orbitals are double-zeta. Two basis functions, one consisting of three Gaussian functions and the other consisting of one Gaussian function, are used to describe the inner and outer parts of each orbital in the valence shell. “G” represents Gaussian

and “d” in parenthesis represents a set of polarization function. It means a single set of d functions is added to the nonhydrogen atoms.

In the basis set 6-311+G(d,p), there are still one basis function consisting of six Gaussian functions for the core orbitals. Each valence orbital is described with three functions, and they are made up of three, one and one Gaussian functions separately. This is a triple-zeta basis set. The “+” means a full set of diffuse s and p functions are added for each heavy (non-hydrogen) atom. The characters in the parenthesis mean for polarization functions, a single set of d function is added to all nonhydrogen atoms and a single set of p function is added to hydrogen atoms. Similarly, in the basis set 6-311+G(2d,p), two sets of d functions are added to the nonhydrogen atoms.

Because of the computational expense and relativistic effects of heavy atoms, simple multi-zeta basis sets are not suitable for them. Effective core potential (ECP) or pseudopotential methods are used for metals. The effects of the core electrons are approximated with an effective potential. LAN2DZ and SDD are among the most widely used ECP methods. LANL2DZ uses the D95V¹⁰ basis set on first row and the Los Alamos ECP plus DZ¹¹⁻¹³ on Na-La, Hf-Bi. SDD uses D95¹⁰ up to Ar and Stuttgart/Dresden ECPs¹⁴ on the remainder of the periodic table.

2.3 SOLVATION MODEL

Solvation can be treated explicitly or implicitly in computations. In the explicit solvation model, solvent is treated as molecules placed around the solute. This is rarely done, since one should really reoptimize for each potential configuration (arrangement in space) of the solvent molecules. In the implicit solvation model, solvent is treated as a continuous polarizable medium surrounding the solute. Computations with implicit solvation models take much less time than those with explicit solvent. In the implicit solvation model, the solute is located in the cavity of

the solvent. The dipole of the solute induces a dipole on the medium around it. When calculating the solvation energy, the shape and the size of the cavity depends on the solute molecule and the solvation method.

PCM, the polarized continuum method, is a commonly used implicit solvation method initially devised by Tomasi and Pascual-Ahuir.¹⁵ The cavity shape of solute with PCM is obtained from the van der Waals radii of the atoms of the solute. There are several different algorithms for PCM solvation model. CPCM, a PCM implementation of the conductor-like screening model,¹⁶ is one of the mostly used versions of the PCM algorithm. It takes the reaction medium as a conducting medium of which the dielectric constant is infinite in calculation, and the solvent dielectric constant is introduced as a correction factor.¹⁷

Another popular continuum solvation model is the SMD solvation model developed by Truhlar, Cramer et al. in 2009.¹⁸ SMD is a solvation model based on the quantum mechanical charge density of a solute molecule interacting with a continuum description of the solvent. In the SMD model, the electrostatic interaction is calculated with the integral equation formalism variant of the PCM algorithm, and non-electrostatic terms are calculated from the effective exposed surface area around the solute and a so-called surface tension. Parameters like the atomic radii used for electrostatic contribution are specified based on empirical numbers in SMD. SMD is a universal solvation model and more accurate than CPCM in most cases.

2.4 INTRINSIC REACTION COORDINATE (IRC) CALCULATION

The intrinsic reaction coordinate (IRC) was proposed by Fukui and is sometimes called the minimum energy reaction path.¹⁹ The intrinsic reaction coordinate is the solution of Lagrange's equation of motion and converges to one of the stable normal coordinates of positive force

constants at the stable equilibrium point and to the unstable normal coordinate of negative force constant at the transition point.²⁰ With the IRC calculation, the steepest descent path from the transition state point is traced along the reaction coordinate until the equilibrium points connecting with the transition state are found on either side of the transition state. The transition state geometry found with the transition state search is usually verified to be connected with reactants and products of interest with IRC calculations.

2.5 PROGRAMS AND FACILITIES

All calculations in this thesis were performed with the Gaussian 09.²¹ Conformation searches were performed with Maestro.²²

Calculations were performed on supercomputer platforms including: Copper and Excalibur provided by the Department of Defense (DoD) High Performance Computing Modernization Program; the UCLA Hoffman2 cluster; and Stampede at the Texas Advanced Computing Center provided by NSF-supported XSEDE.

III. Lactide Ring-Opening Polymerization Catalyzed with the N-Heterocyclic Carbene Catalyst

3.1 INTRODUCTION

3.1.1. Introduction of Polylactides and Polyglycolides

Poly lactide (or polylactic acid, PLA), one of the most promising bio-based materials, has attracted much interest in the past few decades. Because of the availability of the monomer raw material from sugar, as well as their propensity of biodegradability without posing hazard for environment, PLA and derivatives have been widely applied in medicine, often utilized as medical implants and drug carriers.²³

Similar to polylactides, polymers derived from glycolic acid (PGA) are promising constituents of plastics. PGA is a good packaging material used in our daily life, and is also molded into bioassimilable devices for tissue engineering and pharmacy formulation. The property of copolymers (PLGA) are controllable by changing the lactic acid/glycolic acid ratio.²⁴

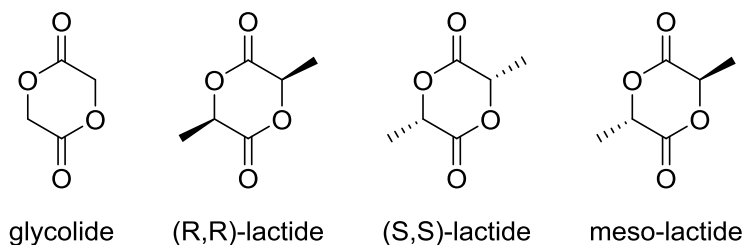
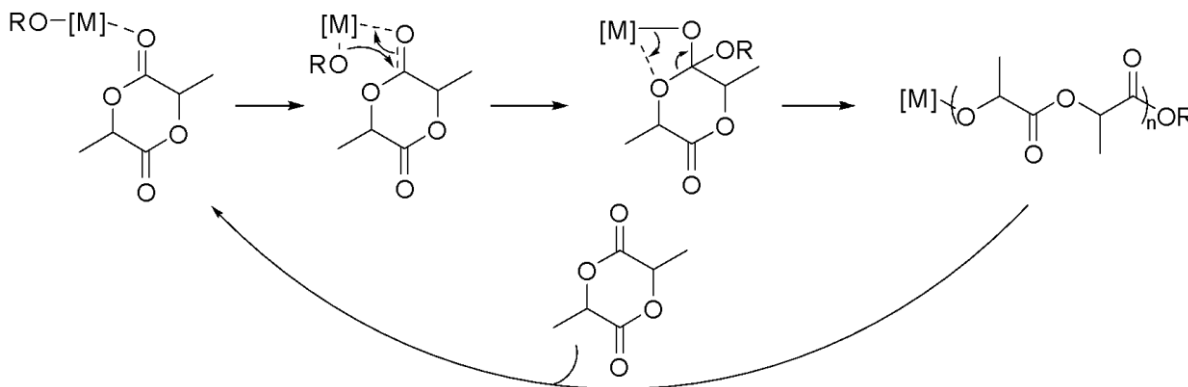


Figure III-1 Structures of glycolide and lactide isomers.

3.1.2. Metallic Catalysts for Ring-Opening Polymerization of Lactide and Glycolide

Nowadays, polymers of lactic acid and glycolic acid are mostly synthesized from the ring-opening polymerization (ROP) of lactide or glycolide (**Figure III-1**). Since pioneering studies by Kleine et al. in 1958,²⁵ various catalysts have been developed.

Metal-based catalysts are widely applied in industry and have been studied extensively. Most of the metal catalyzed ROP of lactide or glycolide involve a coordination-insertion mechanism, supported by both experimental and theoretical studies²⁶. This mechanism consists of three steps. First, the monomer coordinates with metal center. Next, the monomer inserts into the metal-oxygen bond by nucleophilic addition of the metal alkoxide onto the carbonyl carbon. Then, the ring opens through acyl oxygen cleavage releasing a chain end oxygen anion coordinating with the metal. This process can be repeated to form the polymer. (**Scheme III-1**)

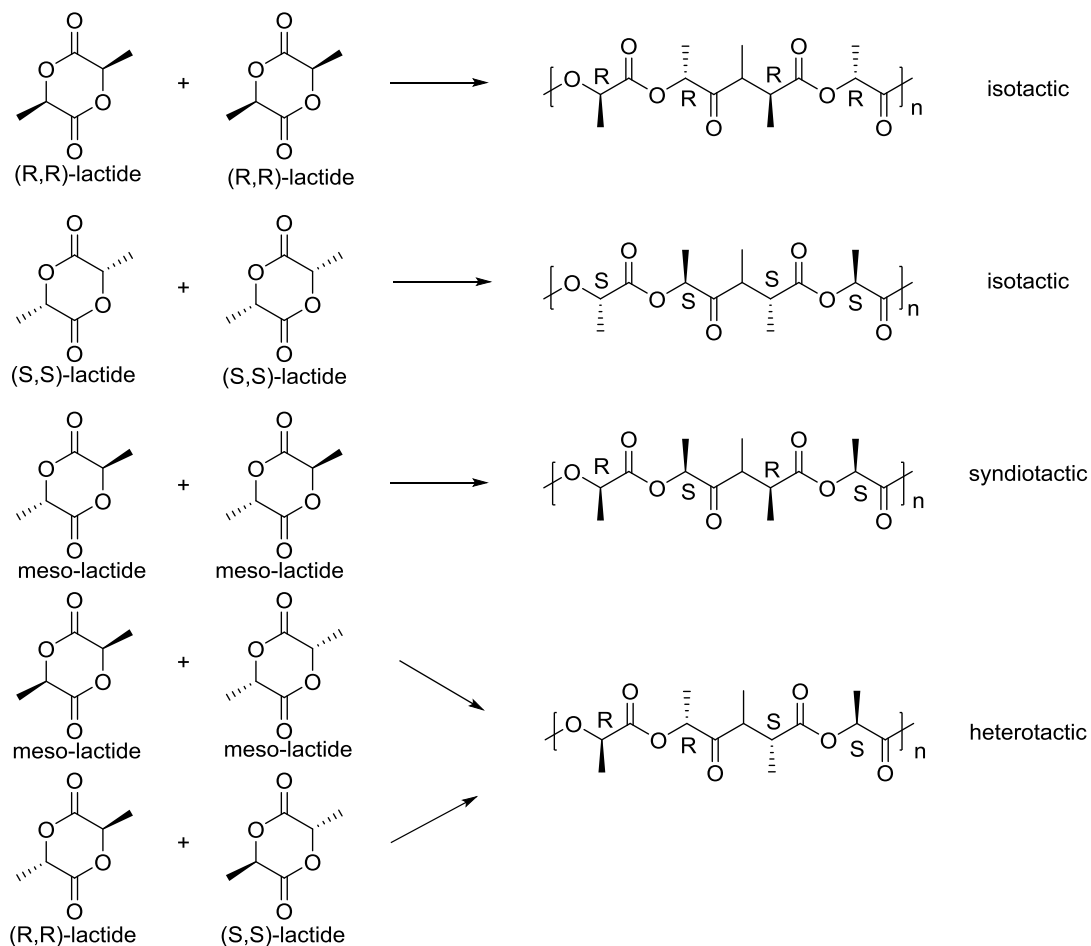


Scheme III-1 General mechanism of metal catalyzed ring-opening polymerization of lactide.

3.1.3. Stereocontrolled Ring-opening Polymerization with Metallic Catalysts

Lactic acid is chiral, while glycolic acid is not. The two enantiomers – L-lactic acid or (R)-lactic acid and D-lactic acid or (S)-lactic acid form three different lactides – (R,R)-lactide, (S,S)-

lactide and the (R,S)- or meso-lactide (**Figure III-1**). Lactides obtained from fermentation of carbohydrates are (S,S)-lactides. Polymerization of enantiomerically pure monomers yields stereoregular isotactic poly[(S,S)-lactide], which has a melting point of 173-178°C. With racemic lactides, isotactic, heterotactic or atactic polymers can be produced with or without stereocontrol.



Scheme III-2 Tacticity of polylactides from different monomers.

Stereoblock isotactic PLA derived from copolymerization of a racemic mixture of (R,R)- and (S,S)-lactides has an increased melting point (180-215°C) which results in more crystalline structures compared to poly[(S,S)-lactide].²³ Alternative and random insertion of enantiomeric (R,R)- and (S,S)-lactides lead to heterotactic and atactic PLA respectively, which have few

applications, because they are amorphous. In the case of meso-lactide polymerization, selective reaction on one stereocenter in propagation results in syndiotactic PLA with a melting point around 153°C. Otherwise, atactic or heterotactic PLA is formed. (**Scheme III-2**)

Stereocontrolled polymerization of lactide has been an interest of chemists for decades. In early years, efforts were concentrated on the chiral ligands on metal center. The initial stereoselective catalysts derive from the work by Sparsky et al.²⁷. They reported that binaphthyl Schiff-base coordinated aluminum catalyst **1** selectively initiates polymerization of (R,R)-LA with

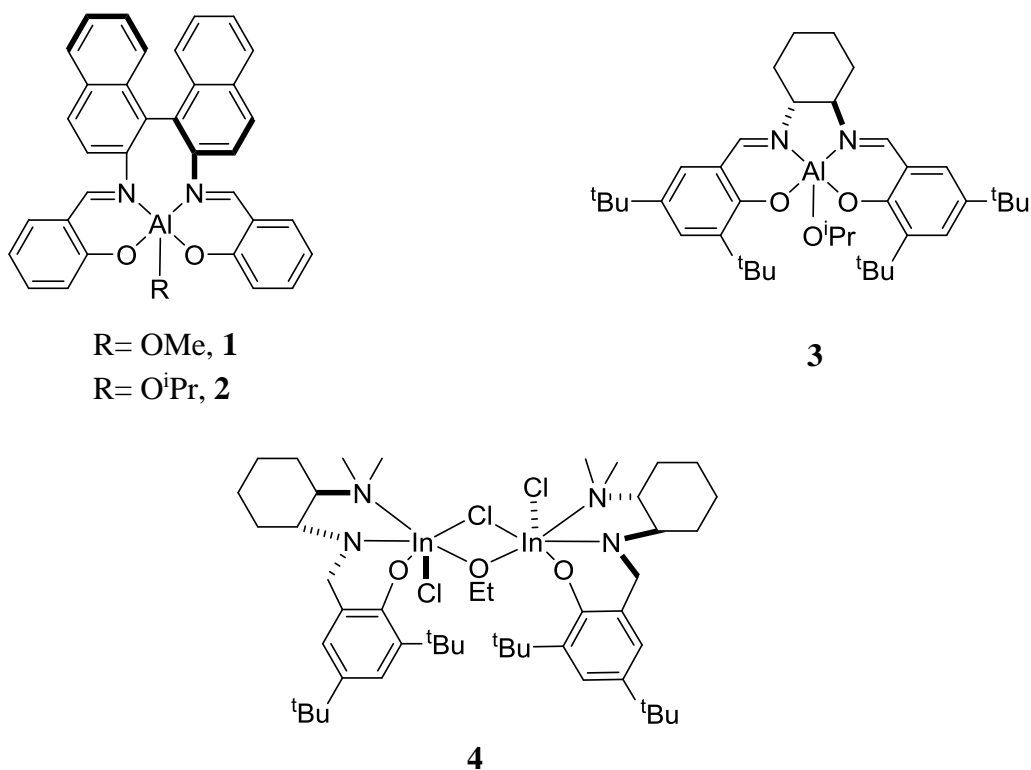
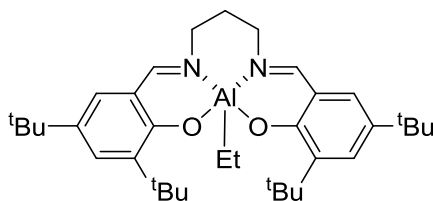


Figure III-2 Stereoselective catalysts with chiral ligands.

rac-LA present. After that, chiral catalysts bearing other metal centers were developed (**Figure**

III-2). Stereo control of polymerization by these catalysts is achieved by the chiral center of the catalysts and the mechanism is so called “enantiomorphic site-controlled”(ESC)²⁸.

Besides chiral catalysts, achiral catalysts can polymerize ROP of lactide as well with steric control through a different mechanism. The first stereoselective metal catalyst bearing an achiral ligand was reported by Nomura et al. in 2002.²⁹ Aluminum catalysts **5** bearing an achiral ligand polymerized rac-LA in an isoselective manner. In 2010s, stereoselective achiral rare-earth catalysts and zinc catalysts were also reported.^{30,31} Because there is no chiral ligand on these catalysts, the stereoselectivity of them derives from the control of inserted monomer in the process of chain growth, thus is named “chain-end-controlled”(CEC) mechanism.



5

Figure III-3 Stereoselective aluminum catalyst with achiral ligands.

3.1.4. Organocatalysts for Ring-Opening Polymerization of Lactide and Glycolide

As noted, medical applications of PLA and PGA are important. However, the metal contaminants can hardly be avoided when metal catalysts are applied in the polymerization. As a result, research into organocatalysts which are free of metal in the whole production process of PLA and PGA is attracting. In the reviews by Waymouth and Hedrick³² and by Bourissou,³³

several types of organocatalysts have been summarized. Selected organocatalysts functioning in polymerization of LA and GA are shown below (**Figure III-4**).

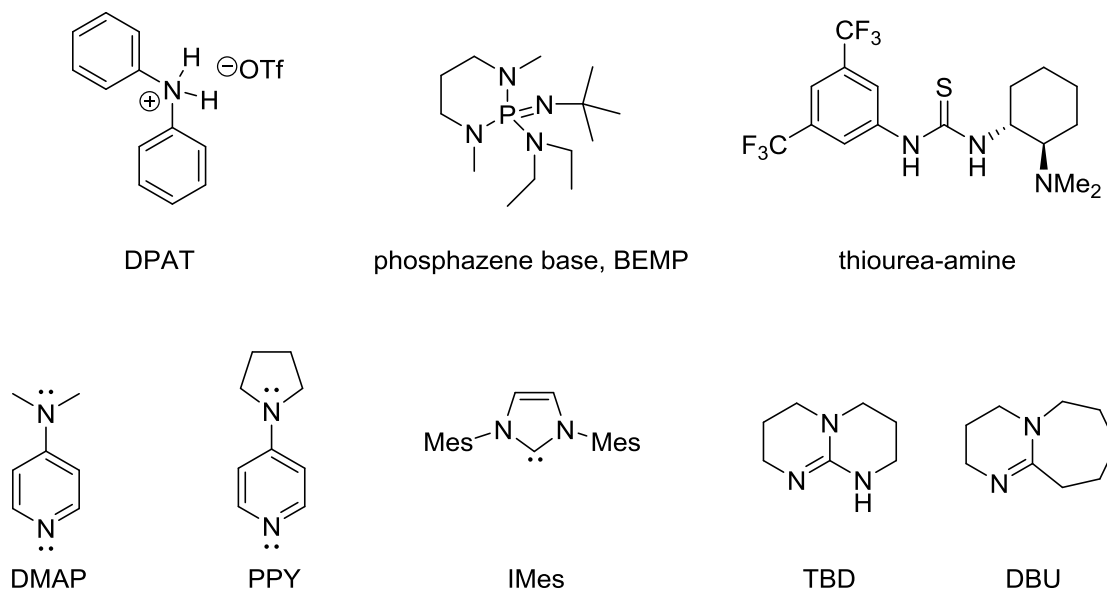


Figure III-4 Typical organocatalysts for ROP of cyclic esters.

Among them, the nucleophilic catalysts are the most studied because of their variability and excellent control of polymerization. The first nucleophilic catalysts, 4-dimethylaminopyridine (DMAP) and 4-pyrrolidinopyridine (PPY), successfully used for lactide polymerization, were reported by Hedrick et al. about fifteen years ago.³⁴ After that, bicyclic guanidine and amidine catalysts such as 1,8-diazabicycloundec-7-ene (DBU) and 1,5,7-triazabicyclo[4.4.0]dec-5-ene (TBD) as well as thiourea-amine and phosphines were also applied to LA polymerization.³⁵⁻³⁸ Motivated by the study of pyridine and phosphine catalysts, ROP catalysis by N-heterocyclic carbenes, which had been promising ligands in organometallic reactions, have been studied extensively since 2006³⁹.

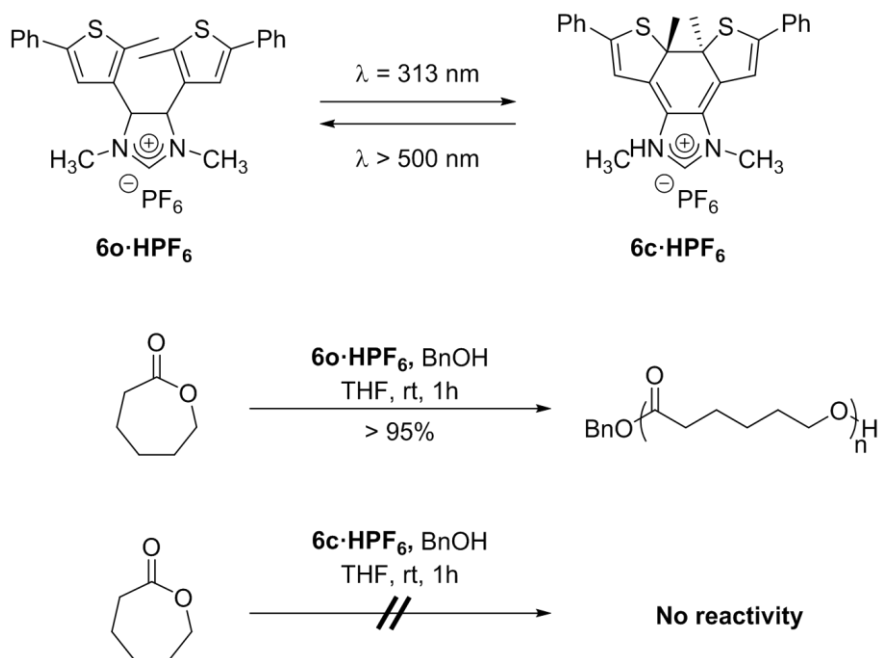
3.1.5. N-Heterocyclic Carbene Catalysts

3.1.5.1. General Introduction

Among all organocatalysts utilized in ROP of lactide, NHCs are one of the most attractive classes of catalysts. NHCs have been found to be powerful metal-free catalyst in organic reactions, especially in ring-opening polymerization.⁴⁰⁻⁴⁴ The first experiment in which NHC was utilized for LA polymerization was performed by Hedrick in 2002. Monodisperse poly(L-lactide) was synthesized by 1,3-bis(2,4,6-trimethylphenyl)imidazol-2-ylidene (IMes, **Figure III-4**) in the presence of alcohol at room temperature.⁴⁵ NHC catalysts with different substituents and saturated carbon backbones were proved to be reliable for LA polymerization with various reactivities.⁴⁶ With versatile NHC catalysts, cyclic polymers, block copolymers and polymers with star or H-shape structures are developed.⁴⁷ Novel materials with special properties can be developed with new structured polymers.

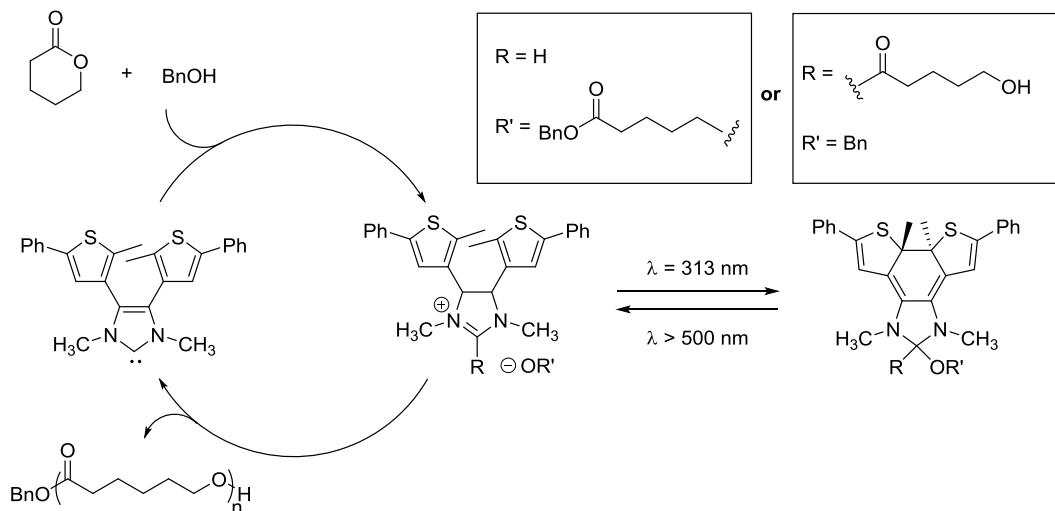
3.1.5.2. Photoswitchable NHC Catalyst

In 2013, Bielawski reported a photoswitchable NHC catalyst with which the ROP of ϵ -caprolactone and δ -valerolactone can be controlled on and off by UV light.⁴⁸ (**Scheme III-3**) Upon



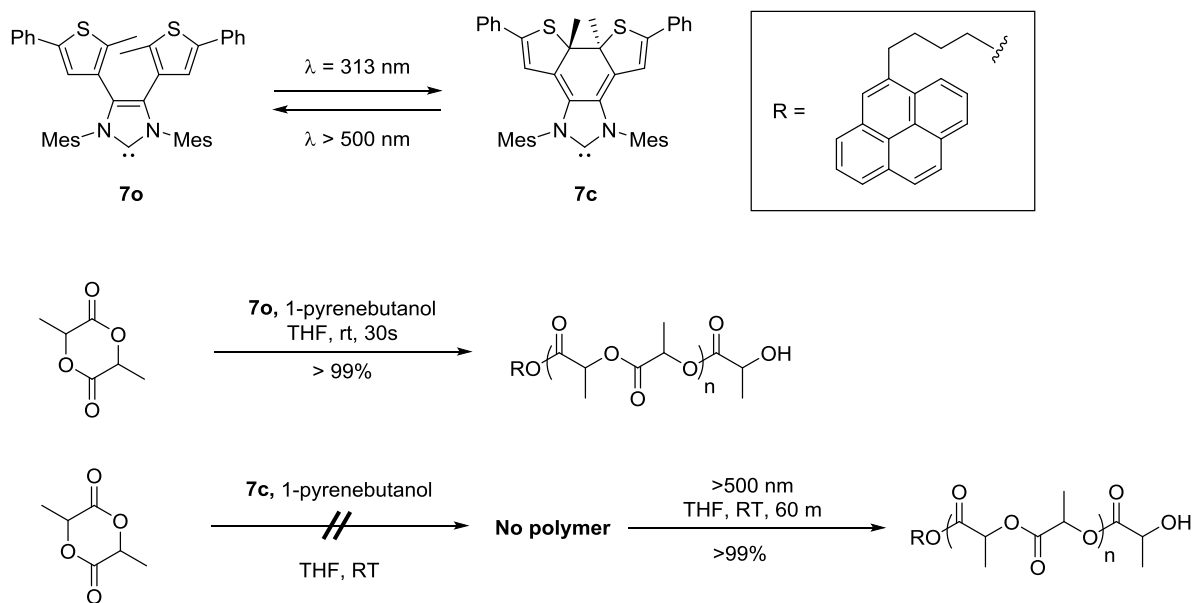
Scheme III-3 Photoswitchable NHC catalyst for ROP of ϵ -caprolactone.

UV light exposure, the NHC **6o·HPF₆** with phenyl substituted thiophene rings attached to C₄ and C₅ undergoes an electrocyclic reaction to form a ring-closed form product **6c·HPF₆**⁴⁹. They found that **6c·HPF₆** shows poor reactivity for ROP of lactones when alcohol is present, whereas **6o·HPF₆** can catalyze the reaction with complete conversion in 1 hour at room temperature. Both **6o·HPF₆** and **6c·HPF₆** are active for the zwitterionic ROP of these lactones in absence of alcohol. With ¹³C NMR, they found that alcohol adducts could be formed with the catalyst under UV light. They



Scheme III-4 Proposed catalytic cycle for a photoswitchable NHC-catalyzed ring-opening polymerization.⁴⁹

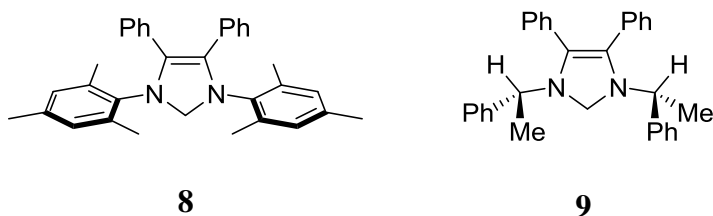
proposed the mechanism shown in **Scheme III-4** to explain these observation. In their later report, they tested the photoswitchable catalyst **7o** with lactide polymerization and observed similar results (**Scheme III-5**).



Scheme III-5 Photoswitchable NHC catalyst for lactide polymerization.

3.1.5.3. Stereocontrol of NHC catalyst in ROP of Lactide

The tacticity of the NHC-catalyzed ROP of LA was reported by Hillmyer and Tolman et al. in 2004.⁵⁰ They observed isoselectivity using IMes for ROP of rac-LA with benzyl alcohol



added. Aiming at gaining more sterically controlled NHC catalysts, Waymouth and Hedrick developed catalyst **8** and **9** to test their performance in lactide polymerization.⁵¹ They found out that both of the achiral and chiral NHCs shows isoselectivity for LA polymerization, and the selectivity increases with lower temperature. They proposed that a chain-end mechanism should be dominant for NHC catalyzed ROP reactions.

3.1.5.4. Mechanistic Studies with NHC Catalyzed Ring-Opening Reactions

Although NHC catalyzed ROP of lactide has been studied by experimentalists for years, systematic theoretical studies are limited, especially compared with the abundance of theoretical papers on organometallic reactions. Experimentally, it was found that NHC catalyzed ROP of LA produces linear product when alcohol is present while cyclic polymers are formed when alcohol is absent. It is widely agreed that the cyclic PLA was achieved through a zwitterionic polymerization where NHC works as the initiator. However, the mechanism of linear PLA production has been

debated for years. Because alcohol is included in the reaction, there are two possible mechanisms, depending on the role of NHC in the reaction, we name one a general-base mechanism although it's often called a hydrogen-bonding mechanism. The second involves nucleophilic catalysis. In the general-base mechanism, NHC performs as a base to deprotonate alcohol which attacks the carbonyl of the monomer. In the nucleophilic mechanism, NHC acts as a nucleophile and directly attacks the carbonyl group of the lactide monomer. To confirm which one is the mechanism for NHC catalyzed ROP reaction of LA, several groups have contributed computational studies in this area. The earliest computational work dates back to the report by Hu et al. in 2005.⁵² They used B3LYP density functional with cc-pVDZ basis set and CPCM solvation model for geometry optimization and larger basis set aug-cc-pVTZ for single point energy calculation. They investigated the reaction between an N-methyl-substituted NHC and methyl acetate with different alcohols to clarify the role of NHC in the reaction. However, in their optimization, the zwitterion produced in the reaction was not stabilized by any other molecules, and dispersion energy was not considered either. Later, Bourissou and colleagues studied the 4-dimethylaminopyridine catalyzed ROP of lactide and concluded that alcohol works as the actual nucleophile in this reaction.⁵³ ROP catalyzed by bicyclic guanidine-based catalyzed was investigated computationally by a collaboration work between Waymouth, Hedrick and IBM.⁵⁴ The general base mechanism is found to be preferred. Nonetheless, a theoretical study with NHC catalyzed ROP reactions was not tackled until 2014 when Gavin Jones at IBM and our former group member, published a paper together with Waymouth et al. reporting their investigation on zwitterionic ring-opening polymerization of δ -valerolactone catalyzed by NHC⁵⁵. Later, they reported their computational results on NHC catalyzed ROP of ϵ -caprolactone with and without alcohol initiator and proved

that the general-base mechanism is preferred by about 6 kcal/mol compared to the nucleophilic mechanism⁵⁶ (**Figure III-5**).

Until now, no computational studies have been done in the case of lactide polymerization with NHC catalyst and issues like stereoselectivity and photoswitchability with NHC catalysts

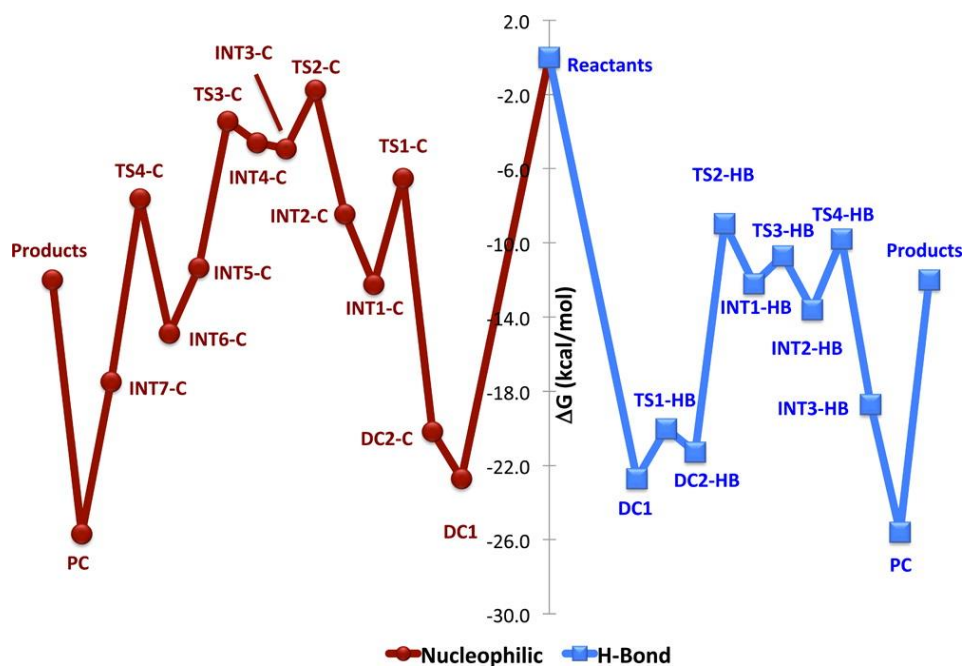


Figure III-5 Reaction pathways and free energies (kcal/mol) for the 1,3,4,5-tetramethylimidazol-2-ylidene catalyzed ring opening of caprolactone in the presence of methanol by the nucleophilic (red) and hydrogen-bonding (blue) mechanisms.⁵⁶

requires more theoretical studies. Inspired by previous experimental and theoretical results as well as the promising prospect of NHC catalysts, we undertook the study of NHC catalyzed ring-opening polymerization of lactide monomers. With the goal of developing a multi-functional NHC catalyst whose stereoselectivity can be switched with environmental factors, mechanisms and

selectivity as well as issues related to Bielawski's photoswitchable catalysts have been studied and will be discussed in detail below.

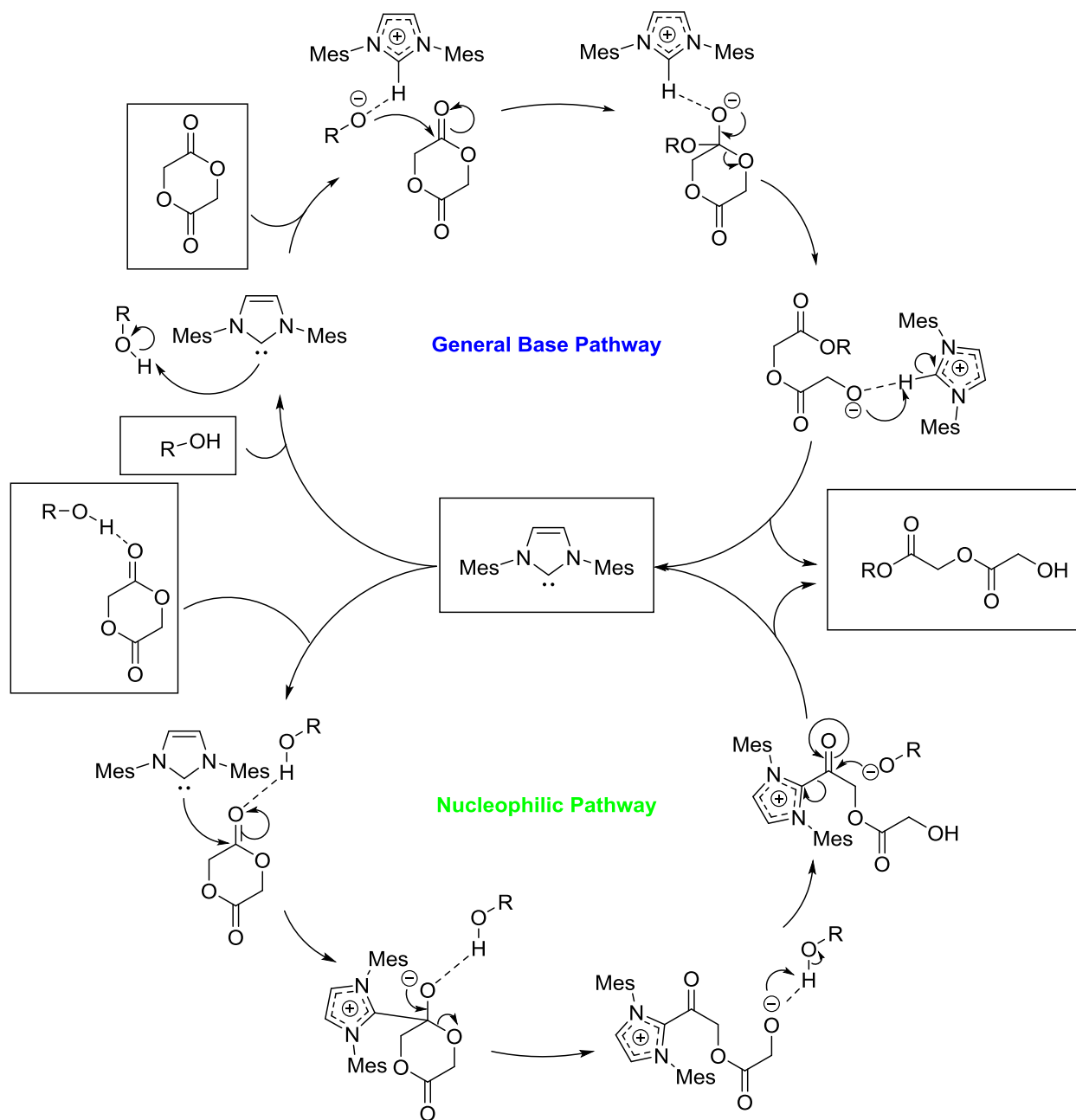
3.2 COMPUTATIONAL DETAILS

The DFT study was performed with Gaussian 09. In this chapter, all geometries were optimized with the hybrid functional and Grimme's dispersion correction, B3LYP-D3⁶ and the 6-31G(d) basis set. Single point calculations were carried out with the same functional and a larger basis set 6-311+G(2d,p). All geometry and energy calculations were performed with the CPCM¹⁶ solvation model for THF. Single point energy calculations with the SMD¹⁸ solvation model were also performed to compare with the results from calculations with CPCM. Intrinsic reaction coordinate (IRC) calculations were performed for transition states.

3.3 RESULTS AND DISCUSSION

3.3.1 NHC-catalyzed Glycolide Polymerization

3.3.1.1 General Base Pathway and Nucleophilic Pathway

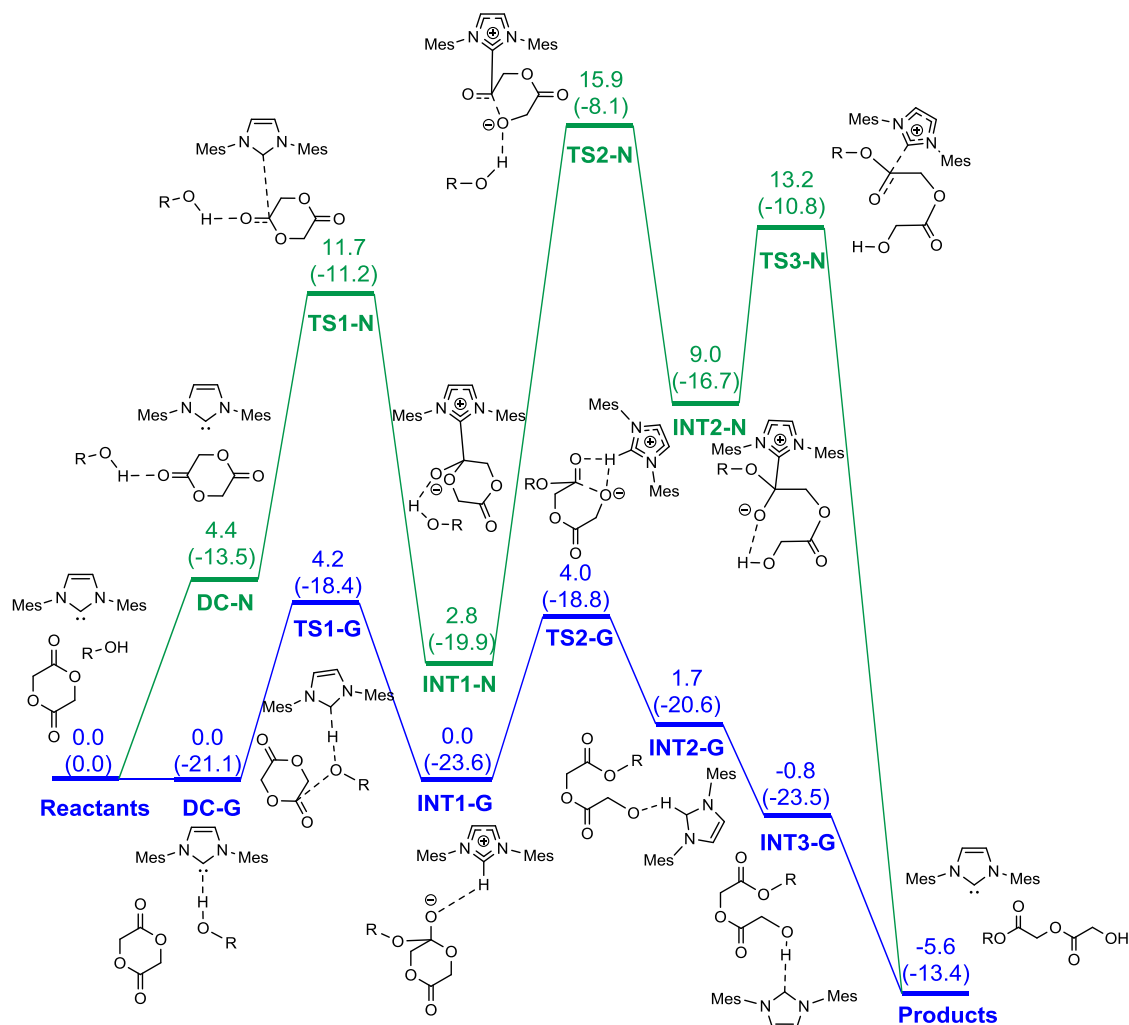


Scheme III-6 General base pathway and nucleophilic pathway. (R=Me in calculation model)

The reactions studied computationally are summarized in **Scheme III-6**. We starts our computation with the reaction of IMes catalyzed glycolide polymerization in the presence of methanol. Glycolide is also a simplified model for lactide without substituents on the ring. IMes is one of the actual NHC catalysts that are widely applied in lactide polymerization. Methanol is the simplified model for the commonly-used benzyl alcohol.

The initiation of ring-opening of glycolide can be activated by both NHC and methanol as they are both nucleophilic. The linear polymerization of cyclic esters in the presence of alcohol is found to be faster than the cyclic polymerization without alcohol. Therefore, alcohol facilitates the reaction, either as the actual nucleophile or by stabilizing intermediates by hydrogen bonding. When alcohol works as the nucleophile, it should be first deprotonated by NHC. In this case, NHC works as a base and this mechanism is called “general base” (G) mechanism. On the other side, when alcohol only functions as proton source and stabilize the anions produced in the reaction, NHC works as a nucleophile to activate the reaction. And this mechanism is called “nucleophilic” (N) mechanism.

The detailed potential energy surface is shown in **Figure III-6** (See next page). The free energies and enthalpies (in parenthesis) of all transition states and intermediates in the most favorable general base and nucleophilic pathways are summarized in it. The general base pathway is shown in blue line and the nucleophilic pathway is shown in green line. All energies are relative to the separate reactants. The reaction is exothermic and the free energy of the products is 5.6 kcal/mol lower than the reactants. Dipole complexes are first formed in both the general base and nucleophilic pathways (**DC-G** and **DC-N**).



B3LYP-D3/6-31G(d) geometry optimization with
 B3LYP-D3/6-311+G(2d,p) single point energy calculation
 and CPCM solvation model in THF solution

Figure III-6 Energy profile of general base pathway (blue) and nucleophilic pathway (green) for IMes catalyzed glycolide polymerization in the presence of methanol. Free energies are shown with enthalpies in parenthesis. All energies are in kcal/mol. R=Me.

In the general base pathway, a hydrogen bond is formed between the alcohol and NHC catalyst (**DC-G**). Then, with the facilitation of NHC deprotonation, the alcohol nucleophilically attacks a carbonyl group of glycolide (**TS1-G**), and forms a stable tetrahedral intermediate (**INT1-G**). After that, the glycolide ring opens with the help of protonated NHC and forms **INT2-G**.

Following proton transfer (**INT3-G**) and NHC dissociation, the polymer is produced and NHC catalyst is regenerated.

In the nucleophilic mechanism, a hydrogen bond is formed between the alcohol and glycolide (**DC-N**). Then, the NHC works as a nucleophile and attacks the hydrogen-bonded carbonyl group of glycolide (**TS1-N**). A tetrahedral intermediate (**INT1-N**) is formed after the nucleophilic attack. Next, the glycolide ring opens with the help of hydrogen bond with alcohol (**TS2-N**) and alcohol reacts with the carbonyl again forming a new tetrahedral intermediate (**INT2-N**). Finally, the NHC dissociates and forms the product.

The overall barrier of general base pathway is only 4.2 kcal/mol whereas the barrier of nucleophilic pathway is 15.9 kcal/mol. So general base pathway is favored for the NHC catalyzed ROP of glycolide.

3.3.1.2 Detailed Discussion on the Energy Profile

The optimized structures of all transition states and intermediates in the general base pathway are shown in **Figure III-7**.

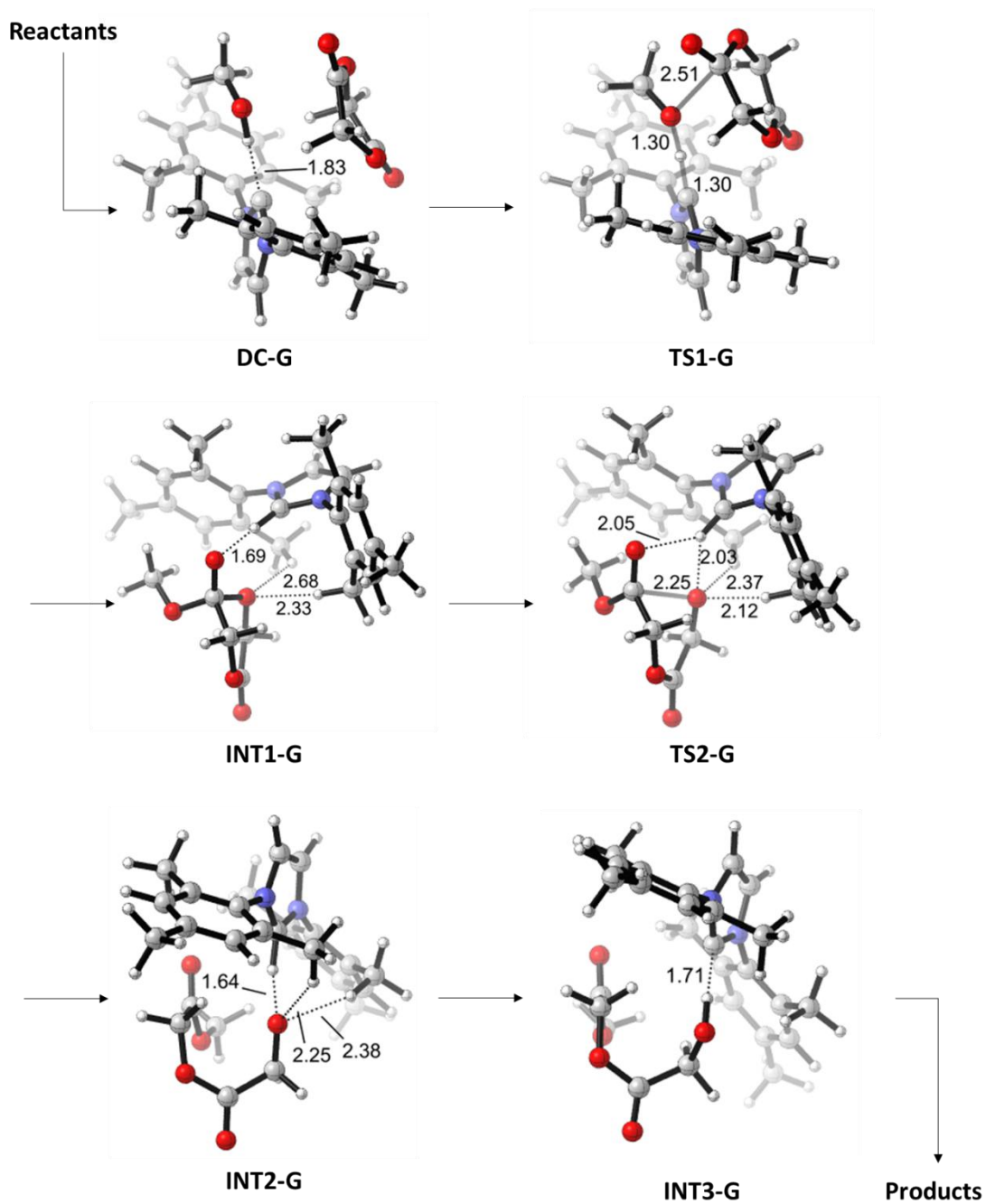


Figure III-7 Optimized structures in the general base pathway.

The optimized structure of glycolide is in boat conformation. In dipole the complex **DC-G**, NHC and alcohol approaches glycolide from the back side of glycolide (**Figure III-8**).

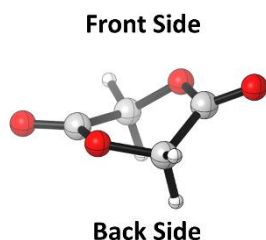


Figure III-8 Optimized structure of glycolide is in boat conformation.

Deprotonation of NHC occurs simultaneously when alcohol attacks the carbonyl group. In **TS1-G**, the glycolide is flat, with a favorable O-C-C-H angle of 173.0° (**Figure III-9**). Because the symmetry of glycolide and its flat conformation in this transition state, there is no difference between nucleophilic attacks from either side of glycolide. In this step, a positive charge is

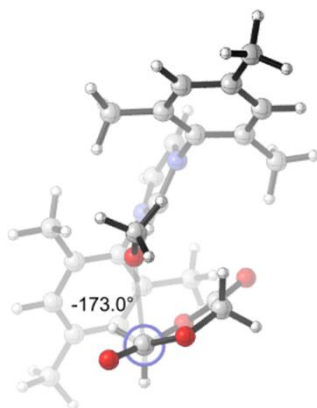


Figure III-9 Transition state conformation of the nucleophilic attack by alcohol

produced on the NHC and a negative charge is produced on the carbonyl oxygen. However, with the proton transfer and nucleophilic attack occurs simultaneously, the transition state is stabilized and the energy barrier is only 4.2 kcal/mol. A stable intermediate **INT1-G** (0.0 kcal/mol) is

produced after the nucleophilic attack and the protonated NHC forms a hydrogen bond with the oxygen anion of the tetrahedral intermediate. This hydrogen bond stabilizes the oxygen anion as well as the positive charged NHC.

When the glycolide ring opens, the hydrogen bond between the carbonyl oxygen and the protonated NHC breaks and a new hydrogen bond forms between the alkoxide anion and the protonated NHC (**TS2-G**). The energy barrier of this step is 4.0 kcal/mol, slightly lower than the first step. The following steps are proton transfer and has low barrier.

The optimized structures of all transition states and intermediates in the general base pathway are shown in **Figure III-10**.

In the nucleophilic pathway, alcohol forms a hydrogen bond with glycolide and the NHC approaches the glycolide from its back side (**DC-N**). With the help of hydrogen bond on carbonyl oxygen, NHC attacks the carbonyl group with a flat conformation of glycolide (**TS1-N**). The energy barrier of the nucleophilic attack by NHC is 11.7 kcal/mol, which is 7.5 kcal/mol higher compared to the nucleophilic attack by alcohol (**Figure III-6**). Although the negative charge of carbonyl oxygen is stabilized by the hydrogen bond with alcohol, there is no stabilization for the positive charge formed on NHC, compared with the general base pathway. The formation of this positive charge leads to the high barrier of the nucleophilic attack step. The second step starts from tetrahedral intermediate **INT1-N** (2.8 kcal/mol). The glycolide ring opens and the alcohol forms a hydrogen bond with the formed alkoxide anion (**TS2-N**). Although the alcohol is positioned close to the NHC, the steric repulsion from mesityl groups inhibits it from providing more stabilization for the positive charge on the NHC ring. The free energy barrier of the ring open is even 4.2 kcal/mol higher than the nucleophilic attack. The last step, dissociation of the NHC catalyst,

requires a free energy of 13.2 kcal/mol, because of the instability of **INT2-N**, which has a positive charge on NHC.

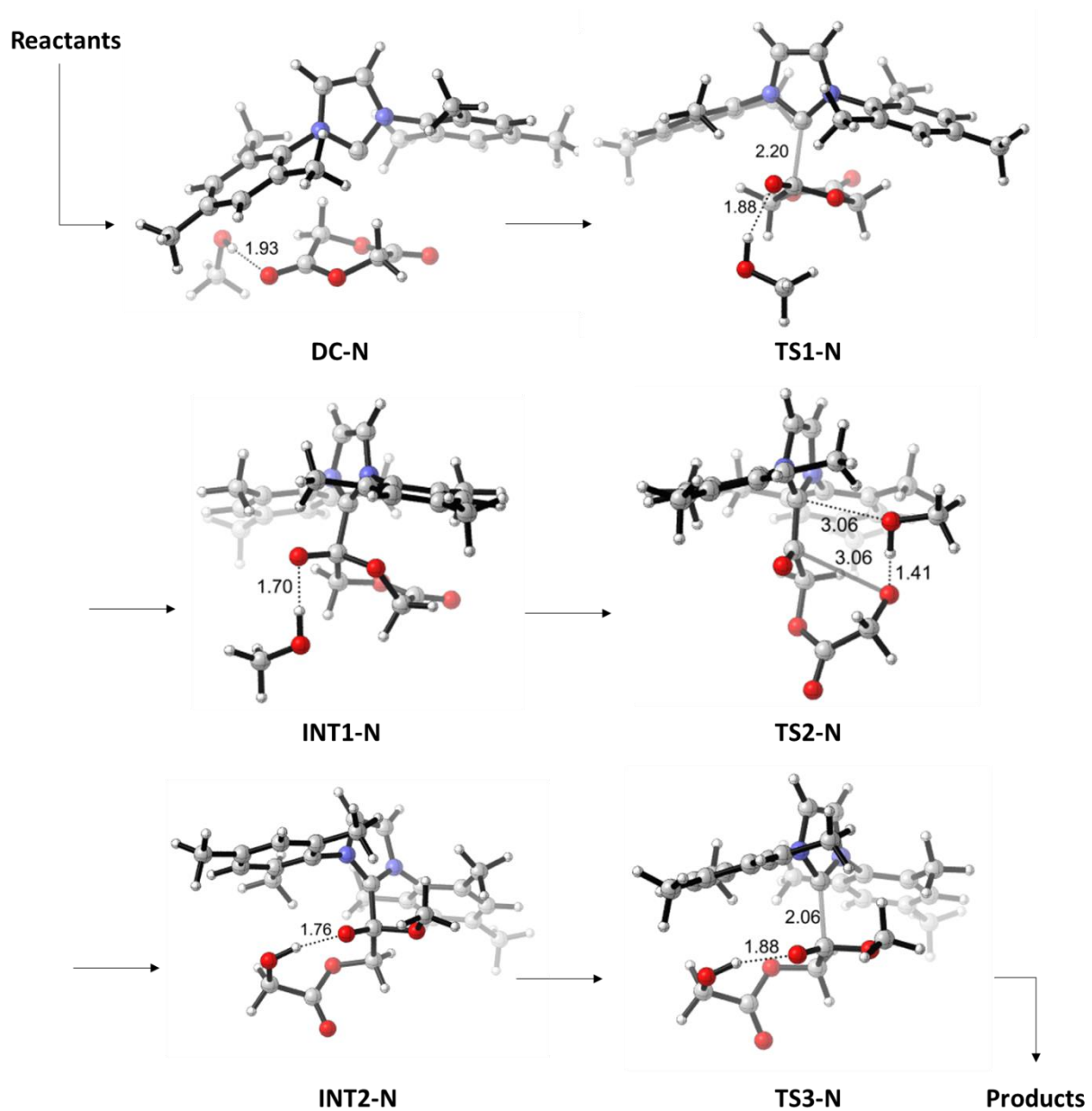


Figure III-10 Optimized structures in the nucleophilic pathway.

The high energy of the nucleophilic pathway is derived from the formation of positive charge on NHC after the initial nucleophilic attack. Although a positive charge is formed on NHC in the general base pathway as well, the hydrogen bond plays an important role to stabilize both the positive charge on NHC and the negative charge on glycolide. However, in the nucleophilic pathway, there is little stabilization observed for the positive charge. As a result, the general base pathway is much more favored compared to the nucleophilic pathway and the ring-opening polymerization of glycolide proceeds through a general base mechanism.

3.3.2 NHC-catalyzed Lactide Polymerization

With the glycolide calculation, the initiation process of lactide polymerization is explored using the same NHC catalyst and methanol as initiator.

The general base pathway is still favored for the lactide polymerization and the optimized structures of the rate determining transition states are shown in **Figure III-11**.

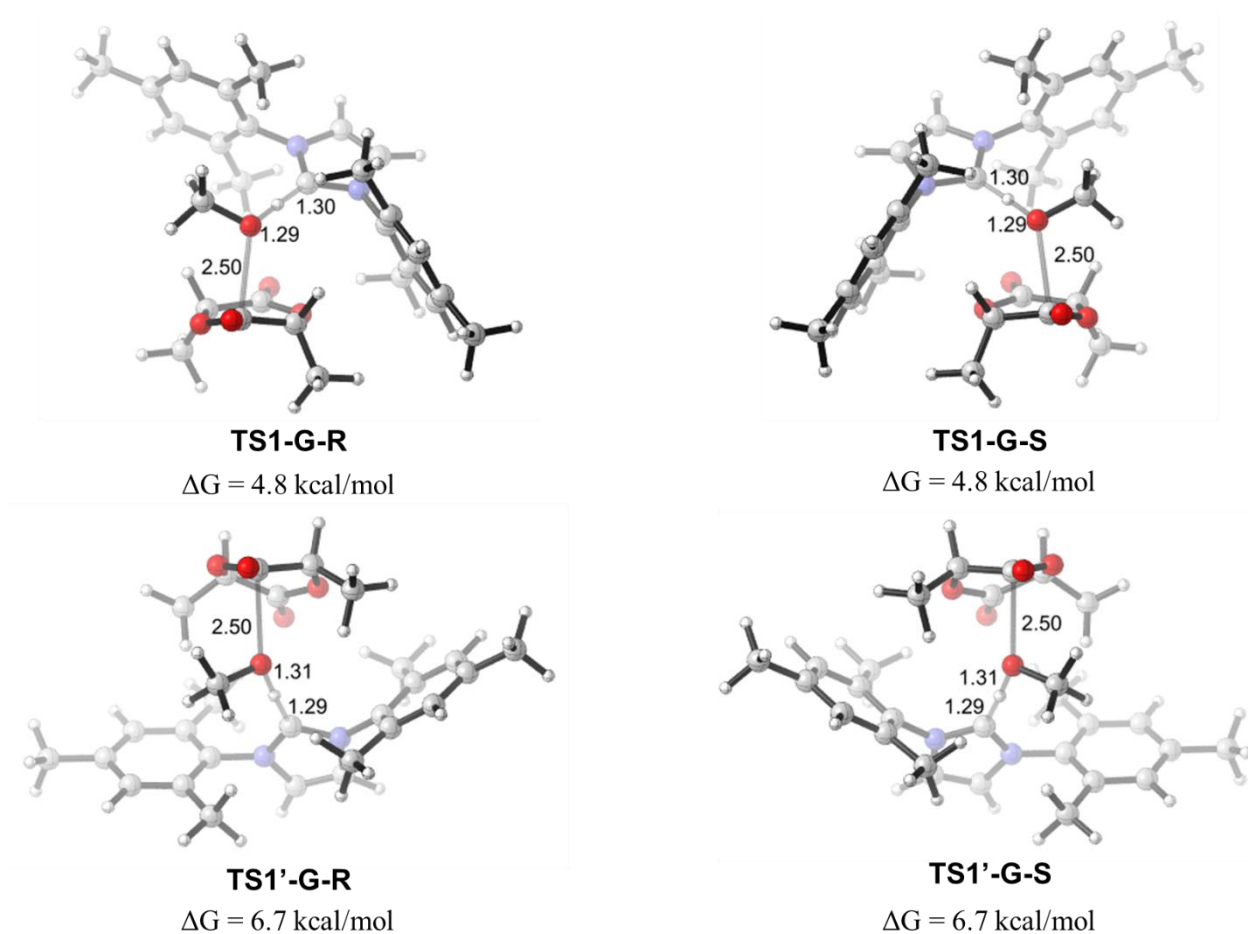


Figure III-11 Optimized structures and free energies of the transition states of the rate-determining step in lactide polymerization.

Alcohol can both attack from the anti (**TS1-G-R** and **TS1-G-S**, top structures in **Figure III-11**) or syn (**TS1'-G-R** and **TS1'-G-S**, bottom structures in **Figure III-11**) position with respect

to the methyl groups of lactide. We found that for both the (R,R)-lactide (**TS1-G-R** and **TS1'-G-R**, left structures in **Figure III-11**) and (S,S)-lactide (**TS1-G-S** and **TS1'-G-S**, right structures in **Figure III-11**), the anti attack requires lower energy barrier than the syn attack. The free energy differences between syn and anti attacks are both 1.9 kcal/mol. The main reason is that there is

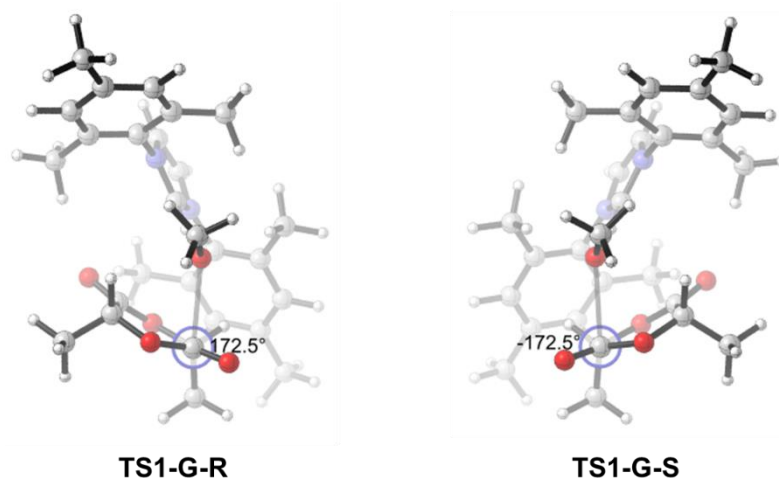


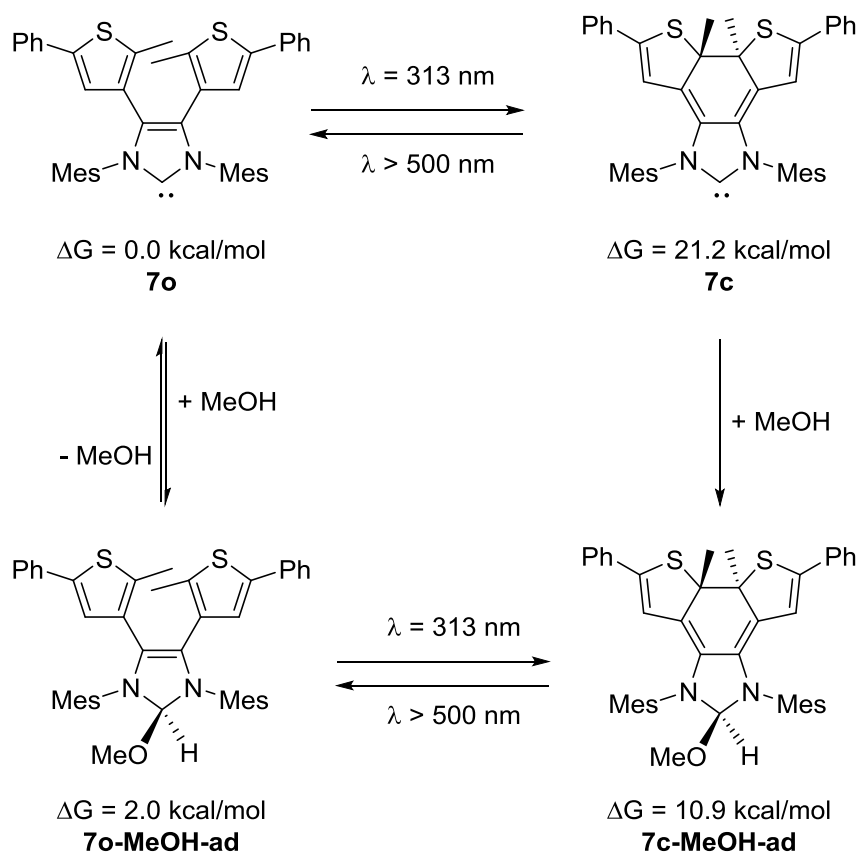
Figure III-12 Anti attack with respect to the methyl group.

less steric repulsion when the alcohol attacks from the anti position of the methyl groups compared to the syn attack. Like **TS1-G** in the glycolide polymerization, the O-C-C-methyl dihedral angles of **TS1-G-R** and **TS1-G-S** are both 172.5° for a favorable nucleophilic attack (**Figure III-12**).

Because the NHC and alcohol model we computed are symmetric, the energy barriers of (R,R)- and (S,S)-lactide polymerization are the same. Both of them are 4.8 kcal/mol. For propagation process, the alcohol is chiral and structures of the transition states will be more complicated.

3.3.3 Theoretical Study on the Photoswitchable NHC Catalysts

The photoswitchable catalysts reported by Bielawski is very important and promising for development of stereoselective NHC catalyst. To understand more about the photoswitchability of these catalysts, mechanism behind experimental observations should be understood. According to Bielawski et al.⁴⁸, alcohol adducts of NHC catalysts play important roles in the process. Using methanol as the model for alcohol, we optimized the structures of both the ring-opened and ring-closed form of the photoswitchable catalyst and their alcohol adducts. Free energies were computed with single point calculations. All calculations are at ground states (**Scheme III-7**).



Scheme III-7 Free energies of the open and closed form of the photoswitchable catalyst and their alcohol adducts.

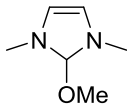
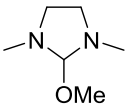
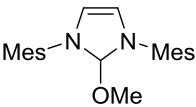
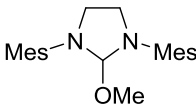
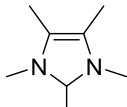
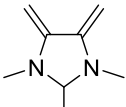
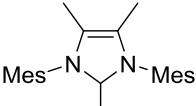
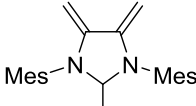
The alcohol adduct of the ring-opened form catalyst, **7o-MeOH-ad**, is 2.0 kcal/mol higher than the free NHC **7o**, and is less stable. However, the free energy of the alcohol adduct of the ring-closed form catalyst, **7c-MeOH-ad**, is 10.3 kcal/mol lower than the catalyst **7c**, and is much more stable.

7c-MeOH-ad is so stable that when alcohol is present with **7c**, the alcohol adduct will be easily produced and the reaction is exergonic and not reversible. However, when it comes to **7o**, the alcohol adduct has higher energy compared with the free initiators so the formation of alcohol adduct is endergonic and quite reversible. Consequently, **7c** cannot catalyze the ring-opening polymerization in the presence of alcohol whereas **7o** catalyzes the reaction well. When UV light is applied during the reaction of ROP of lactide with **7o** in the presence of alcohol, **7c** is produced and quickly reacts with alcohol molecules to form alcohol adduct. The reaction then stops because the catalyst is “deactivated” or “off”. When visible light is applied, adduct **7c-MeOH-ad** undergoes ring-opening reaction similar to **7c** and generate **7o-MeOH-ad**. This new adduct easily decomposes and free NHC catalyst **7o** and alcohol is reproduced. Therefore, NHC catalyst is “reactivated” or “on”. In conclusion, the formation of the stable alcohol adduct makes the ring-closed form catalyst inactive for ROP.

To explain why the energy of the alcohol adduct of closed-form Bielawski catalyst has such low energy compared to the free catalyst, model studies on simple NHC catalysts were carried out (**Table III-1**).

It can be found that the alcohol adducts of unsaturated NHC catalysts are less stable than the free NHCs (**10-13**). When the NHC ring is saturated, the alcohol adducts are less stable (**14, 15**). In particular, when there are two double bonds attached to the NHC ring, the alcohol adducts are more than 10 kcal/mol more stable than the free NHCs (**16, 17**).

Table III-1 Relative free energies of NHC alcohol adducts.

NHC-adduct	ΔG (kcal/mol)	NHC-adduct	ΔG (kcal/mol)
 10	6.6	 14	-4.5
 11	5.3	 15	-2.6
 12	6.9	 16	-10.8
 13	10.9	 17	-11.4

The reason why the alcohol adducts **10-13** are more stable than the free catalyst is that the free NHC rings are aromatic whereas the alcohol adducts are nonaromatic. The free NHC rings of **14** and **15** are nonaromatic and the carbenes are not as stable as those of **10-13**. So their alcohol adducts are more stable. For **16** and **17**, the double bonds are electron withdrawing by conjugation with the p orbital of nitrogen and makes the nitrogen atoms have less electron donation effect for the vacant p orbital of carbene carbon. Therefore, the free NHCs of **16** and **17** are much less stable compared to the unsaturated NHCs. Because of the instability of the free NHCs, the alcohol adducts are easy to be produced and are quite stable. The formation of this low-energy adducts makes the double-bond-attached NHCs inactive for polymerization.

The situation is similar for the ring-opened and ring-closed form NHC catalysts. When the ring is open, the NHC ring is aromatic and stable. The alcohol insertion is not favored to occur.

However, after ring closing, the electronic arrangement on the NHC changes and it is no longer aromatic. Electrons on the unsaturated bonds attached to the NHC ring conjugates with p electrons of N, making N atoms less electron-donating and the carbene is destabilized. The unstable NHC can easily undergo alcohol insertion reaction and form a relative stable adduct. As a result, it can no longer catalyze the ROP of lactide.

3.3.4 Solvation Model Comparison

We also carried out single point calculations with SMD solvation model for all of the results in this chapter. The comparison of results for the free energy calculation with glycolide are shown in **Table III-2**.

Table III-2 Free energies in NHC catalyzed ROP of glycolide by CPCM and SMD solvation model.

	General Base Pathway		Nucleophilic Pathway		
	ΔG (kcal/mol)		ΔG (kcal/mol)		
	CPCM	SMD	CPCM	SMD	
Reactants	0.0	0.0	Reactants	0.0	0.0
DC-G	0.0	5.4	DC-N	4.4	9.5
TS1-G	4.2	10.0	TS1-N	11.7	17.9
INT1-G	0.0	5.9	INT1-N	2.8	9.1
TS2-G	4.0	9.2	TS2-N	15.9	21.8
INT2-G	1.7	8.1	INT2-N	9.0	16.0
INT3-G	-0.8	5.0	TS3-N	13.2	19.7
Product	-5.6	-5.3	Product	-5.6	-5.3

The free energies of the intermediates and transition states calculated by SMD solvation model are typically 5-7 kcal/mol higher than the free energies from the CPCM calculation. The free energies of the product by the two solvation models are close (only 0.3 kcal/mol difference). Geometry optimization with SMD model were also performed and the optimized structures are very identical to structures optimized by CPCM solvation model. The major difference within the results by SMD and CPCM solvation models is from energy.

To figure out whether the free energy difference comes from enthalpy or entropy calculation, we also compared the enthalpy results from both the two solvation models (**Table III-3**). The difference within enthalpies calculated from CPCM and SMD solvation models are

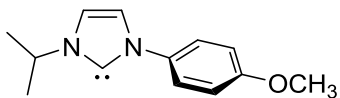
Table III-3 Enthalpies in NHC catalyzed ROP of glycolide by CPCM and SMD solvation model.

General Base Pathway			Nucleophilic Pathway		
	ΔH (kcal/mol)			ΔH (kcal/mol)	
	CPCM	SMD		CPCM	SMD
Reactants	0.0	0.0	Reactants	0.0	0.0
DC-G	-21.1	-15.7	DC-N	-13.5	-8.4
TS1-G	-18.4	-12.6	TS1-N	-11.2	-5.0
INT1-G	-23.6	-17.7	INT1-N	-19.9	-13.6
TS2-G	-18.8	-13.6	TS2-N	-8.1	-2.3
INT2-G	-20.6	-14.2	INT2-N	-16.7	-9.8
INT3-G	-23.5	-17.7	TS3-N	-10.8	-4.3
Product	-13.4	-13.1	Product	-13.4	-13.1

similar to the differences within the free energies. So the energy differences by CPCM and SMD calculations come from enthalpy calculation.

Although the free energies from SMD calculation are different from the results from CPCM, the conclusions drawn from the calculations by both the two solvation models are the same. With CPCM solvation model, the free energy of **TS1-G**, the rate limiting transition state in the general base pathway, is 11.7 kcal/mol lower than **TS2-N**, the rate limiting transition state in the nucleophilic pathway. With SMD solvation model, the free energy of **TS1-G** is 11.8 kcal/mol lower than the free energy of **TS2-N**. So the general base pathway is always favored no matter which solvation model is used.

No accurate experimental kinetic studies have been carried out to give information for this specific reaction. However in 2013, Wang et al. measured the rate of ROP of lactide catalyzed by **18** and reported an activation energy of 12.0 kcal/mol.⁵⁷ Computational studies with other NHC



18

catalysts were also carried out by us and results shows that the reaction barriers are quite different between NHCs in different sizes (**Table III-4**). However, all calculated NHC catalysts go through

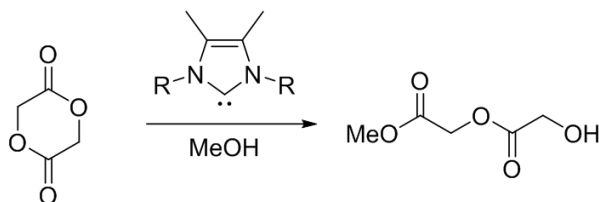


Table III-4 Free energies calculated with different N-substituents.

R	TS1-G	TS1-N
-CH ₃	7.4	12.2
-CH ₂ CH ₃	5.2	12.3
-CH ₂ CH ₂ CH ₃	6.3	11.3
-CH(CH ₃) ₂	4.0	13.4
-Mesityl	3.4	5.6

a general base mechanism for glycolide polymerization. The highest barrier calculated with CPCM solvation model among these catalysts is 7.4 kcal/mol which is 4.6 kcal/mol lower than the experimental results. Although SMD calculation has not been carried out for these NHC catalysts, we predict that the free energy barriers from SMD calculations should be higher than the CPCM

results based on the calculation with IMes. So the results calculated with SMD solvation model should be more accurate.

3.4 CONCLUSION

In this chapter, we calculated the free energy barrier for both of the general base and nucleophilic mechanism of NHC catalyzed glycolide polymerization. Results show that general base pathway is more favored. The reason is that in the general base mechanism, the positive charge on the NHC is stabilized by the hydrogen bonds formed between the oxygen anions and the protonated NHC. The rate determining step is the nucleophilic addition of glycolide by alcohol.

Mechanism calculations of lactide polymerization were carried out and the general base mechanism is also favored. Because both the NHC and alcohol we used in the simulation are symmetric, the energy barrier of (R,R)-lactide and (S,S)-lactide polymerization are the same.

We also investigated the photoswitchable NHC catalyst. The alcohol adduct of the ring-closed form catalyst is quite stable and lead to the inactivity of the catalyst under UV light. When the alcohol is present, the ring-closed catalyst reacts with alcohol and forms an alcohol adduct. When visible light is applied, it undergoes a ring-opening reaction and the alcohol adduct of the ring-opened catalyst is not stable. The free catalyst is regenerated and participate in the catalysis of ROP of the substrate.

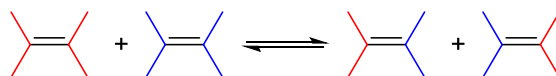
In the future, we will continue our study on the stereoselectivity of NHC catalyzed ROP of lactide. Detailed mechanism of the propagation process will be studied with chiral alcohol model. The energy barrier of the (R,R)- plus (R,R)- propagation and (R,R)- plus (S,S)- propagation will be compared. With computational results, chiral photoswitchable catalyst which can selectively catalyze the ROP of one enantiomer of racemic substrate will be developed.

IV. Initiation with Z-Selective Ruthenium Catalysts – Mechanism and Anionic Effects

4.1 INTRODUCTION

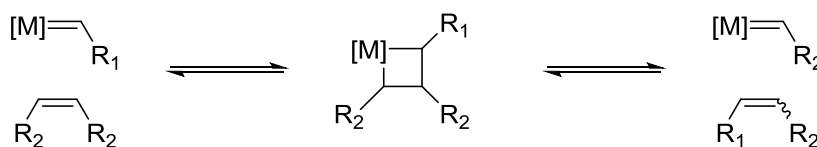
4.1.1 Olefin Metathesis

4.1.1.1 Background



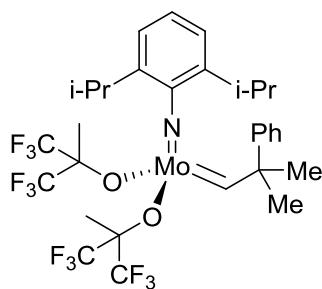
Scheme IV-1 Olefin metathesis reaction.

Olefin metathesis (**Scheme IV-1**), one of the most facile reactions in organic synthesis was first discovered in 1950s during the process of industrial olefin polymerization. Although transition metals were known as catalysts for this reaction, the mechanism was not clear until 1971 when French scientist Yves Chauvin proposed the metallacyclobutane mechanism by which a lot of experimental observations in olefin metathesis could be explained.⁵⁸ In this mechanism, the olefin molecule first coordinates with the catalytic metal center bearing a carbene ligand. Next, through a four-member ring transition state, a metallacyclobutane intermediate consisting of the metal and carbon atoms from the olefin and carbene is formed. The ring then undergoes a ring opening reaction to switch the “partners” and produce a new olefin and a new metal carbene. (**Scheme IV-2**)



Scheme IV-2 A four-member ring intermediate is formed during olefin metathesis according to Chauvin's mechanism.⁵⁸

The discovery of olefin metathesis makes it possible that the double or triple bonds inert under regular conditions can couple with each other and expands how the organic frameworks could be constructed. The reaction can occur at room temperature without harsh conditions and tolerates most functional groups. As a result, olefin metathesis quickly attracted the attention of academia and industry as soon as it came up.⁵⁹



19

Figure IV-1 One of Schrock's molybdenum catalysts.

In the early studies on olefin metathesis catalysts, tantalum, tungsten and molybdenum catalysts were all found to be active. The first well-defined highly active catalysts where Mo or W works as the central metal atom were reported by Schrock et al. in 1990s after about twenty years of effort testing different metal catalysts (**Figure IV-1**).⁶⁰ These catalysts require milder conditions compared with previous analogues. However, limitations still exist because of their sensitivity towards air and moisture, as well as intolerance of some functional groups.

4.1.1.2 Ruthenium Catalysts for Olefin Metathesis

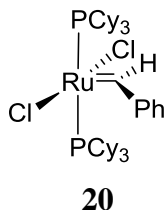


Figure IV-2 The first generation of Grubbs catalyst (**G1**).

In 1992, a well-defined ruthenium complex which catalyzes the ring-opening metathesis polymerization (ROMP) of norbornene was reported by Grubbs et al.⁶¹ The catalysts initiate the reaction at room temperature and resist water, alcohols and carboxylic acids. Other Ru catalysts were developed later. **Figure IV-2** shows the structure of one of these which is practical in laboratory synthesis. These catalysts are named as Grubbs' catalysts, and the catalyst in **Figure IV-2** is the first generation of Grubbs' catalyst (**G1**) which was first reported in 1995⁶². Four years later, the second generation of Grubbs catalysts was synthesized, where an imidazolin-2-ylidene (NHC) ligand coordinates with ruthenium⁶³ (**Figure IV-3**). It shows higher reactivity and selectivity in catalysis of olefin metathesis reactions.

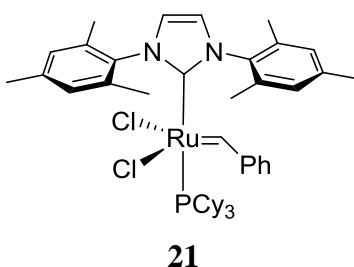
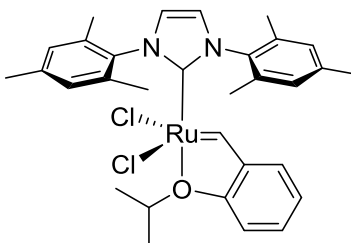


Figure IV-3 The second generation of Grubbs catalyst (**G2**).

Although the catalyst efficiency of **G1** and **G2** is high, their thermal stability is not ideal, and they decomposes easily under higher temperature. Amir H. Hoveyda et al. introduced a benzylidene ligand with a nucleophilic ortho-isopropoxy group chelated with Ru attached to the

benzene ring and increased the catalyst stability remarkably. Grubbs' catalysts bearing the Hoveyda ligand are so called Hoveyda-Grubbs catalysts (**Figure IV-4**).^{64,65}

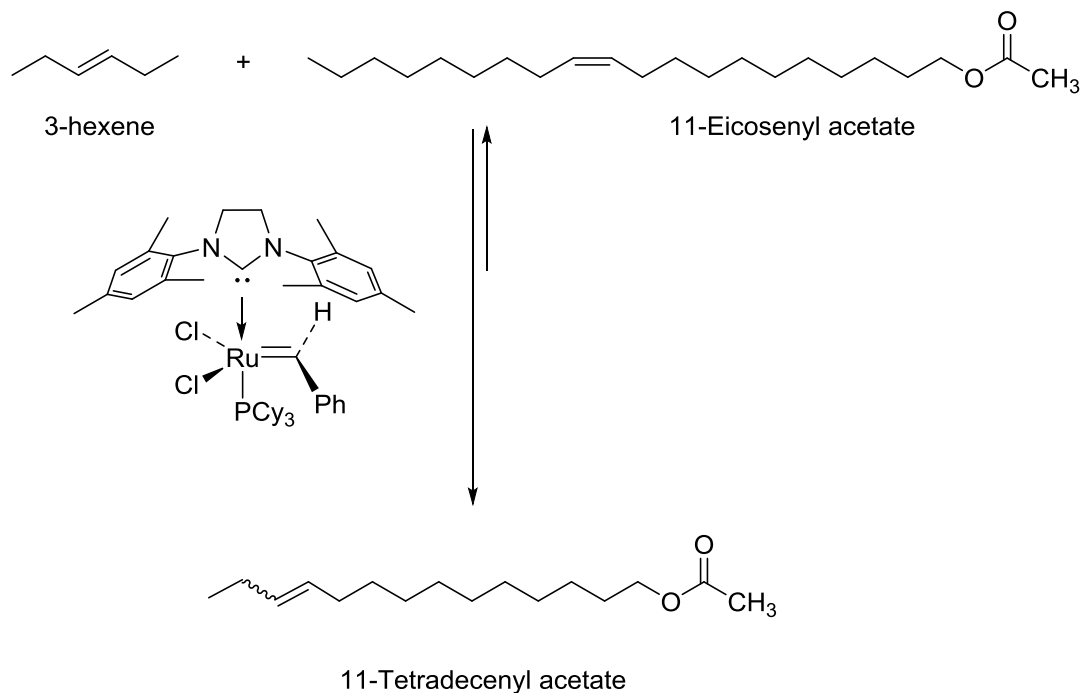


22

Figure IV-4 Hoveyda-Grubbs catalyst (**GH2**).

Grubbs catalysts have the advantage of high reactivity and selectivity under mild reaction conditions with good functional tolerance. They have now been the most popular catalysts for olefin metathesis reactions in organic synthesis.

Since the discovery of olefin metathesis, new organic molecules can be made with the metathesis reaction. Not only because of its facility and high yield, but also because it is one of the best examples of “green chemistry”, olefin metathesis has become one of the most promising organic reactions in chemical synthesis. The 2005 Nobel Prize of Chemistry was awarded to Chauvin, Schrock and Grubbs to commend their contribution in this area. The reaction has been widely applied in the materials, pharmaceutical and biotechnology industries.



Scheme IV-3 Synthesis of insect pheromones with olefin metathesis.⁶⁶

Scheme IV-3 shows an application of olefin metathesis with the 2nd generation of Grubbs catalyst.⁶⁶ The accessible 3-hexene and 11-eicosenyl acetate are used to synthesize 11-tetradecenyl acetate, the major component of Omnivorous Leafroller pheromone. In addition to pheromones, pesticides, additives of polymer fuel and functional polymer materials can be synthesized through olefin metathesis. Furthermore, olefin metathesis is an effective method to synthesize pharmaceuticals.

4.1.2 Z-Selective Olefin Metathesis

Because of thermodynamic stabilities, the E-product is always favored over Z-product in olefin metathesis. To satisfy the demand of product synthesis containing Z- double bonds, catalysts selectively producing Z-olefins have intrigued scientists in the last few years.

4.1.2.1 Molybdenum and Tungsten Z-Selective Catalysts

The first Z-selective olefin metathesis catalyst was reported by Schrock and Hoveyda et al. in 2009.⁶⁷ Molybdenum-based monoaryloxide-pyrrolide (MAP) species, **23** (Figure IV-5),⁶⁸ which contains “large” aryloxide and “small” imido ligands, was utilized as initiator in several

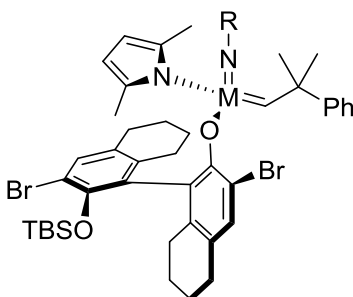


Figure IV-5 Molybdenum or tungsten based MAP Z-selective catalysts. M=Mo (**23**) or W (**24**), R=adamantyl or 2,6-dimethylphenyl.

olefin metathesis reactions. High Z-selectivity and excellent yield was achieved for the ring-opening metathesis polymerization (ROMP) of dicarbomethoxynorbornadiene, cyclooctene and 1,5-cyclooctadiene. Later, MAP catalysts were successfully applied in Z-selective homocoupling of terminal olefins⁶⁹ and natural product synthesis.⁷⁰ Tungsten MAP catalysts and other molybdenum based Z-selective catalysts were reported by them as well.⁷¹

4.1.2.2 Ruthenium Z-Selective Catalysts

Comparing to Mo and W catalysts, as aforementioned, Ru catalysts are not only tolerant towards diverse functional groups but also can be synthesized easily. As a result, it was important to develop ruthenium based catalysts for Z-selective olefin metathesis for wider utility. The development of Z-selective Ru olefin metathesis catalysts was achieved in 2011 by Grubbs group.^{72,73} Their novel catalyst derives from the second generation of Hoveyda-Grubbs Catalyst **25** (Figure IV-6). With the help of silver pivalate, the C-H bond of methyldene group on adamantyl

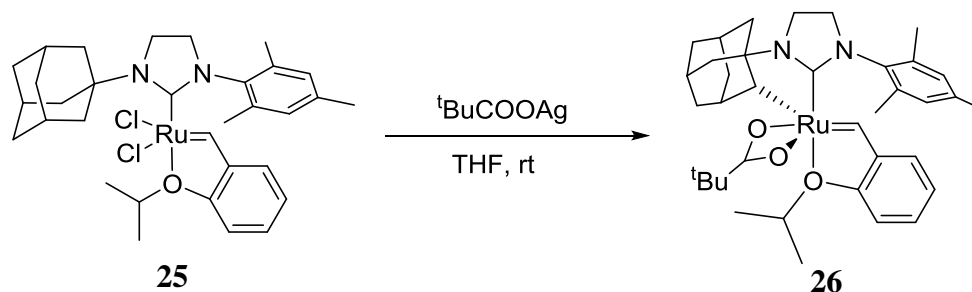


Figure IV-6 Synthesis of ruthenium Z-selective catalyst.

substituent of NHC ligand is activated and forms a carbon-ruthenium bond to produce catalyst **26**. The “chelated” catalyst, **26** is able to catalyze the cross metathesis reaction of allylbenzene and cis-1,4-diacetoxy-2-butene with an E/Z ratio of 0.12. The results for homodimerization of terminal olefins are even better with more than 95% Z-product.⁷³

With modification of the anion ligands, N-substituents of NHC ligand, NHC backbones and Hoveyda ligand, conversion and Z-selectivity have been achieved not only in traditional olefin synthesis such as ROMP and cross metathesis but also in allylic and diol olefin.⁷⁴⁻⁸⁰

The mechanism of Ru catalyzed Z-selective olefin metathesis was clarified with DFT study by Houk group with collaboration with Grubbs.⁸¹ In comparison with the bottom-bound pathway by **G2** catalysts (**Figure IV-7**), olefin metathesis with chelated Ru catalysts undergoes a side-

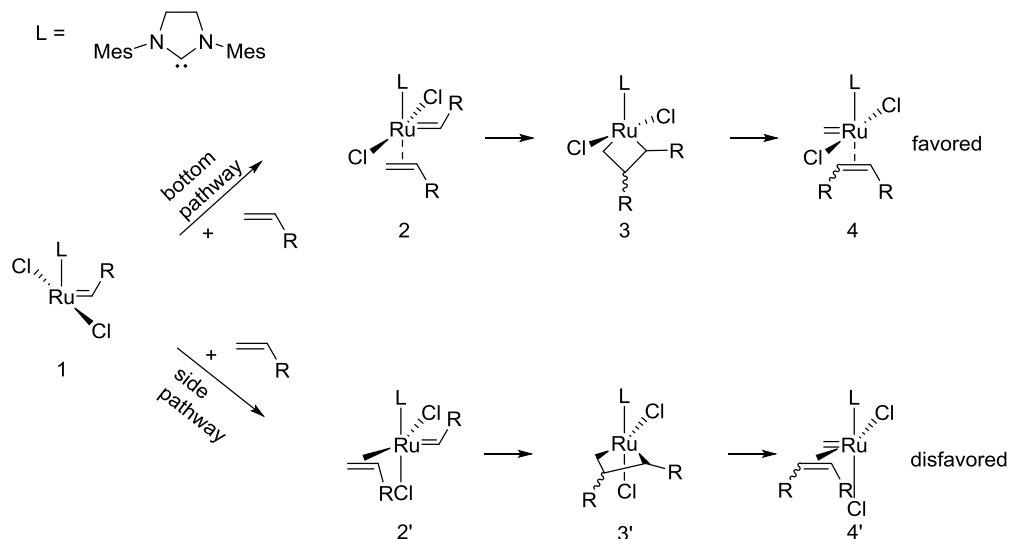


Figure IV-7 Bottom-bound pathway is favored for Grubbs II catalysts.

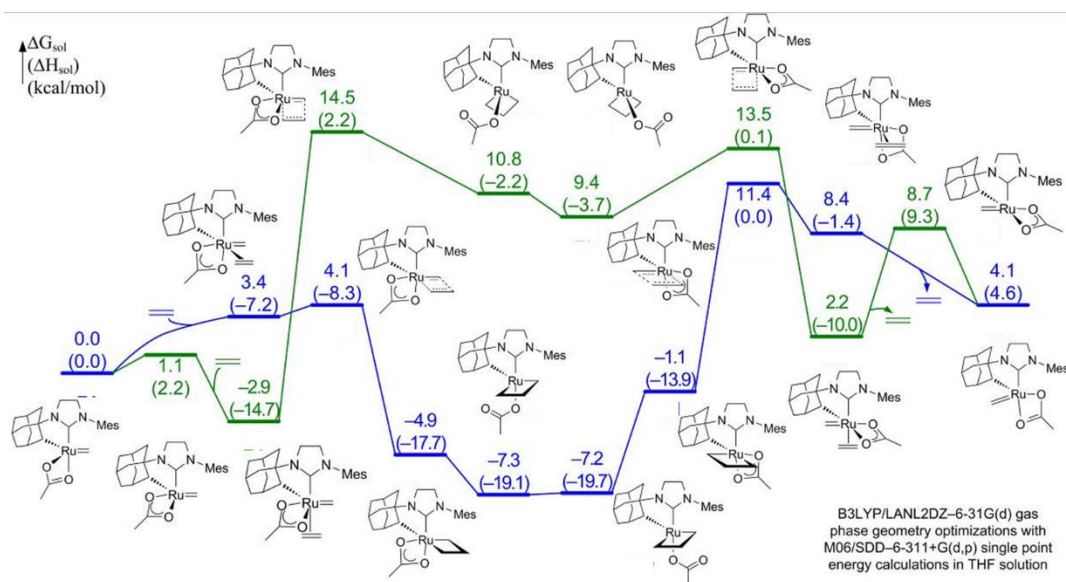


Figure IV-8 Side-bound pathway is favored for chelated Ru catalysts with DFT calculation.⁸¹

bound pathway in which the olefin coordinates with the ruthenium from the side direction (**Figure IV-8**).

The side-bound pathway is favored mainly because chelation of N-substituents with ruthenium fixed the orientation of NHC ligand, resulting in strong π -back donation of Ru toward NHC and the alkylidene carbon in the bottom-bound pathway transition states.

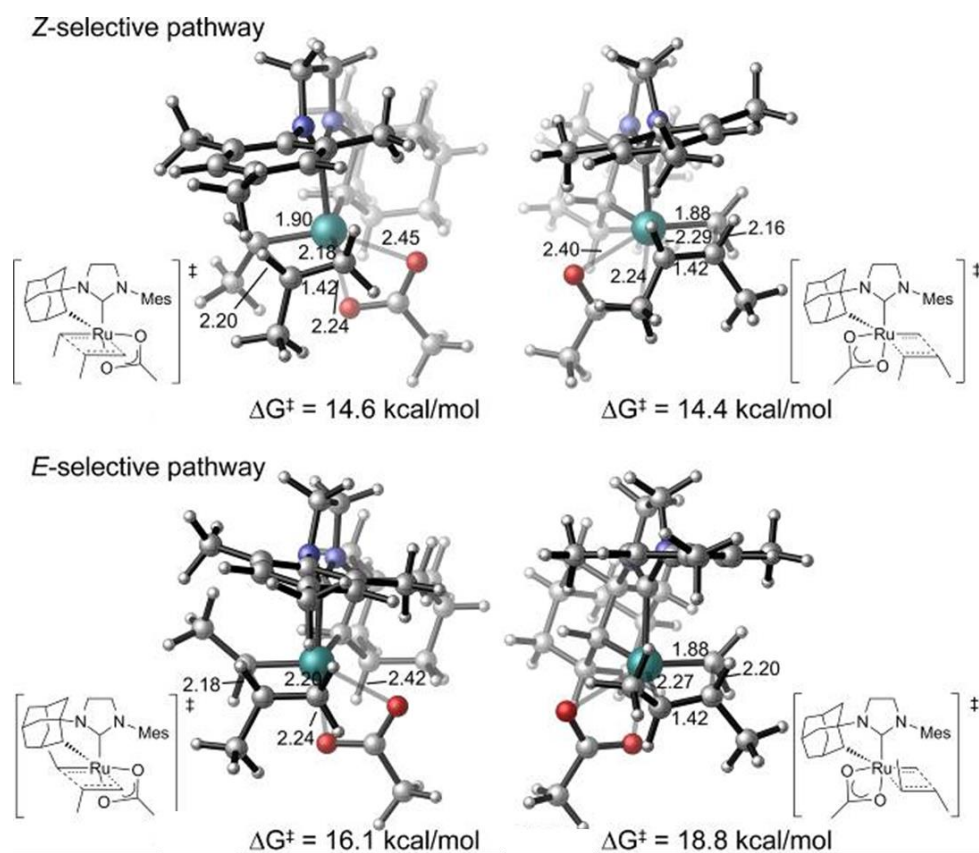


Figure IV-9 Energy and optimized structures of transition states in Z-selective and E-selective pathways.⁸¹

In the side-bound mechanism, there is repulsion between the N-substituting mesityl group and the metallacyclobutane intermediate and the four-membered ring transition states. Consequently, geometries with substituents pointing down away from mesityl group are preferred

when there are substituents on the reacting olefin and alkylidene (**Figure IV-9**). The preference for this geometry leads to lower energies of transition states in the *Z*- pathway of olefin metathesis compared with those in the *E*- pathway. Consequently, the chelated ruthenium catalysts show high *Z*-selectivity in olefin metathesis reactions.

Although *Z*-selectivity was successfully explained in this paper, the initiation process was not discussed. Grubbs et al. reported that with modification of ligands, the initiation rate of chelated ruthenium catalysts varies considerably.⁷³ An investigation into the initiation process was undertaken to help understand the mechanism and guide catalyst development.

4.1.3 Initiation Mechanism with Ruthenium Olefin Metathesis Catalysts

4.1.3.1 Initiation Mechanism of the Second Generation of Grubbs Catalysts

Studies on initiation of Grubbs catalysts have been reported with both experiment and theory. According to Sanford et al. in 2001, Grubbs-II catalysts undergoes a dissociation mechanism in the initiation process.⁸² First the phosphine ligand dissociates from the ruthenium center reversibly, exposing a coordinatively unsaturated ruthenium to coordination of olefin. The olefin then forms metallacyclobutane intermediate through the four-membered ring transition state, and undergoes subsequent steps to produce the product. The rate determining step in the initiation process is the dissociation of phosphine ligand, and this mechanism is called “dissociative mechanism” as result. (Figure IV-10)

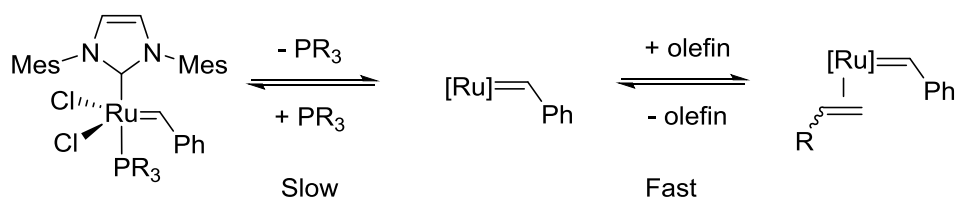


Figure IV-10 Grubbs II catalysts undergoes dissociation mechanism for catalyst initiation.

However, for Hoveyda-Grubbs (**GH**) catalysts, the initiation mechanism could be complex. According to the experimental work by Plenio and colleagues, an associative mechanism occurs in the initiation process of **GH** catalysts.⁸³ Detailed mechanistic studies were first performed by Plenio, who found that initiation rates of **GH** catalysts were influenced by the nature and concentration of the alkene substrate with kinetic studies.⁸⁴ DFT studies were later carried out by Percy and Hillier. They investigated three possible mechanisms: dissociative, interchange and

associative. The dissociative mechanism resembles the S_N1 reaction. The ortho-isopropoxy ligand first dissociates from the ruthenium atom and then the olefin coordinates with the metal. The rate determining step is the dissociation of the ligand. The interchange mechanism resembles the S_N2 reaction. The olefin substrate coordinate with ruthenium when the dissociation of ortho-isopropoxy ligand occurs simultaneously. The associative mechanism resembles the nucleophilic addition reaction. The substrate first coordinates with ruthenium to form a coordinatively saturated intermediate, and then the ligand dissociates from the metal. The rate determining step is the coordination of the olefin substrate. According to their reports, the interchange mechanism was proved to be the one which has the lowest barrier among all three possible mechanisms.⁸⁵ In the next year, Plenio et al. published their detailed study with different substrates and pre-catalysts, and concluded that dissociative and interchange mechanism are both possible in the initiation process depending on the alkene and pre-catalyst.⁸⁶ A computational study by Solans-Monfort et al. however ruled out the associative mechanism,⁸⁷ but the entropy estimate was not accurate in that study. Subsequent computational studies by Hillier and Percy demonstrated that the formation of metallacyclobutane could have a barrier higher than the dissociative or interchange initial steps in the initiation process and the initiations kinetics of **GH2** catalysts are substrate dependent.⁸⁸

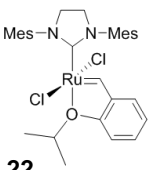
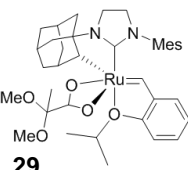
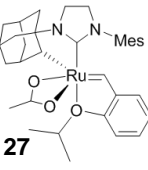
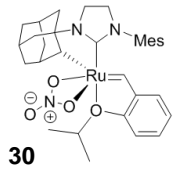
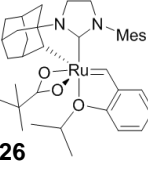
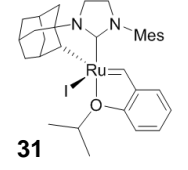
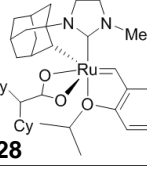
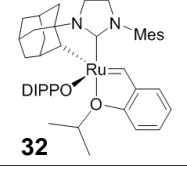
4.1.3.2 Initiation Studies on Z-Selective Ruthenium Catalysts

Because the special chelation pattern of the Z-selective Grubbs catalysts, initiation steps are thought to be different from previous Grubbs-Hoveyda catalysts. Computational studies could be helpful for development of fast initiating, stable catalysts.

Grubbs and co-workers reported the experimental initiation rates with different chelated ruthenium catalysts.⁸⁹ Butyl vinyl ether was used as the substrate since the produced ruthenium

alkoxymethylidene is inactive for subsequent olefin metathesis. Selected initiation rate constants are shown in **Table IV-1**.

Table IV-1 Initiation rate constants with various ruthenium catalysts.*

Catalyst	Temp, °C	Initiation rate constant, 10^{-3} s^{-1}	Catalyst	Temp, °C	Initiation rate constant, 10^{-3} s^{-1}
	30	7.2 ± 0.2		30	2.5 ± 0.1
	30	0.17 ± 0.04		30	0.84 ± 0.03
	30	0.87 ± 0.02		50	0.17 ± 0.01
	30	6.9 ± 0.3		70	<0.39

*Rate constants of reactions with butyl vinyl ether.

Initiation rate constants vary a lot from $0.2\text{-}7 \times 10^{-3} \text{ s}^{-1}$ with different anionic ligands. Chelated ruthenium catalysts have comparable initiation rate constant with non-chelated second generation Hoveyda-Grubbs catalysts. With an increase on size of the anionic ligand, initiation rates increases significantly (**27**, **26**, **28**). This indicates that a simple associative should not be correct, because in the associative mechanism, increasing the steric bulk of the carboxylate should result in a decrease in the initiation rate constant. Electron-donating anionic ligands accelerates by

a factor of 3 when two methoxyl groups replace the methyl substituents on the α -carbon of pivalate ligand (**29**). Ruthenium catalysts with nitrate ligand (**30**) have similar initiation rate constant to those with carboxylic ligands, although they show better overall reactivity for the homocoupling reactions. Interestingly, the initiation rates with complexes with monodentate anionic ligands (**31**, **32**) are much smaller, even at high temperatures. Catalysts with monodentate ligands are found to be metathesis inactive.

DFT studies were carried out by Wang et al. to clarify the overall mechanism with chelated Ru catalysts.⁹⁰ They calculated the dissociative pathway and found that the ring-opening step after alkene forms metallacyclobutane with ruthenium alkylidene has a higher energy barrier compared to the dissociation of the alkoxyphenyl ligand.

Since no detailed comparison has been reported for associative, interchange and dissociative pathways before, we have used computational method to explore how the chelated ruthenium catalysts differ from Hoveyda-Grubbs catalysts. In addition, the difference in initiation rates with catalysts coordinated with different anionic ligands are studied with theoretical study. The inactivity of monodentate catalysts was also investigated.

4.2 COMPUTATIONAL DETAILS

All geometry optimizations, frequency and energy calculations in this chapter were carried out with DFT methods using Gaussian 09. Geometries were optimized with hybrid functional B3LYP in gas phase. The LANL2DZ basis set were used for ruthenium and 6-31G(d) for other atoms. Vibrational frequencies were calculated to verify the stationary points. Intrinsic reaction coordinate calculations were performed to for transition state structures. All calculated transition states were justified by checking the single imaginary frequency and the corresponding vibrational mode.

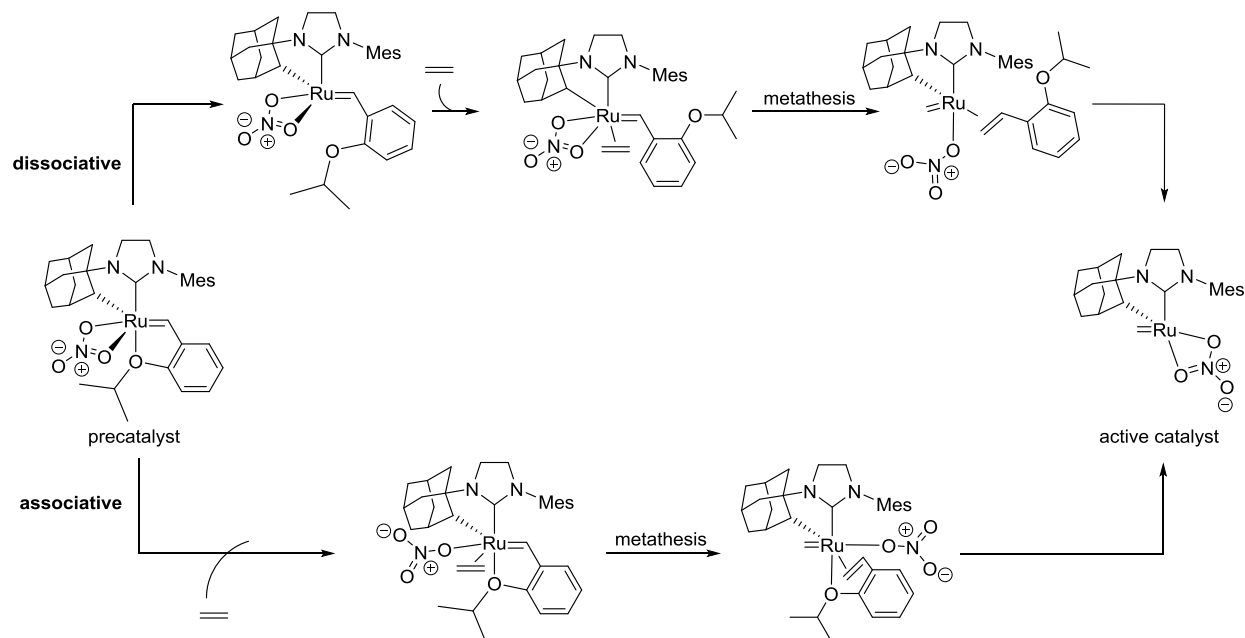
Single point calculations were carried out with M06⁷ in THF with SMD¹⁸ solvation model. The SDD basis set (D95 up to Ar and Stuttgart/Dresden effective core potentials on the remainder of the periodic table) for ruthenium and iodide and 6-311+G(d,p) for other atoms was utilized. Free energies and enthalpies were calculated by the single point electronic energy corrected with the thermal correction from previous B3LYP/LANL2DZ/6-31G(d) calculations. All of the free energies and enthalpies in this chapter are the absolute values relative to the unreacted pre-catalyst and reactants.

4.3 RESULTS AND DISCUSSION

4.3.1 Initiation Mechanism of Z-selective Ruthenium Catalysts

According to previous study on the initiation of the 2nd generation Hoveyda-Grubbs catalysts (GH2), the Z-selective catalysts could initiate with an associative, interchange or dissociative pathway. The oxidation number of Ru in the Z-selective catalyst **30** is 4, the same as in the previous 2nd generation Hoveyda-Grubbs catalysts. The major difference from previous GH2 catalysts is that its ruthenium is six coordinated whereas the previous GH2 catalysts are five-coordinated. The Z-selective catalysts have 18-electron coordinative sphere. As a result, the initiation process cannot occur without any dissociation of the ligands.

Because the initiation process includes the metathesis of the Hoveyda ligand with substrate olefin, the dissociation of the Hoveyda ligand is important in the initiation, and involves a



Scheme IV-4 Dissociative and associative mechanism.

dissociative mechanism. The olefin coordinates with ruthenium after dissociation of the Hoveyda ligand. (Scheme IV-4)

The olefin could also coordinate with ruthenium before the Hoveyda ligand dissociates. In this case, one oxygen on the nitrate ligand has to dissociate also. Here dissociation of ligand occurs first, and we call this an associative mechanism, because the olefin substrate associates with ruthenium before the dissociation of Hoveyda ligand.

An interchange mechanism, in which the olefin coordinates with ruthenium simultaneously as the Hoveyda ligand dissociates, can also be proposed. However, we think it is not theoretically possible, because of the steric hindrance by other ligands. Only the dissociation and associative mechanism as defined above, were considered.

4.3.1.1 Dissociative Mechanism

In the dissociative mechanism, the chelating ortho-isopropoxy group first dissociates from the ruthenium. The olefin then coordinates with the catalyst and undergoes an olefin metathesis reaction.

4.3.1.1.1 Dissociation of the Ligand

The ortho-isopropoxy group can dissociate from the ruthenium through a rotation of the alkylidene-aryl C-C bond (red arrow in **Figure IV-11**).

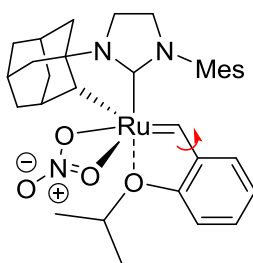


Figure IV-11 Dissociation of ligand through bond rotation.

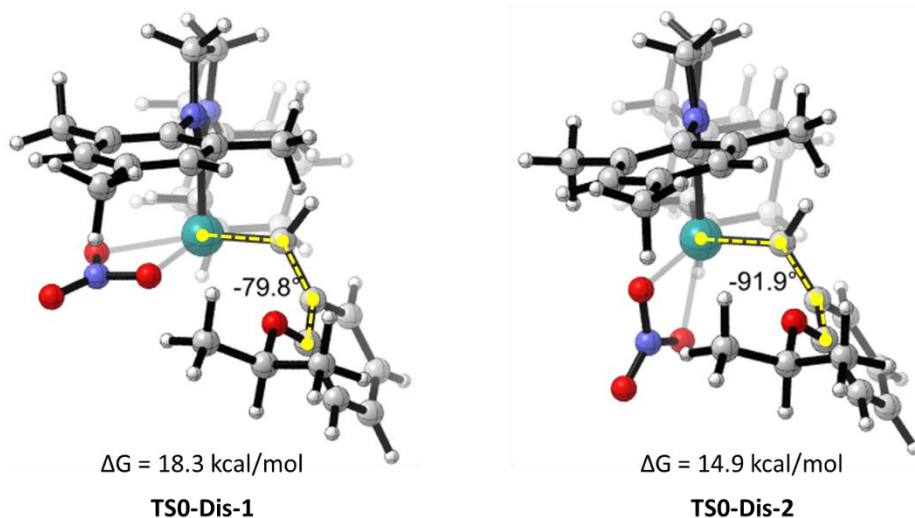


Figure IV-12 Transition states of ortho-isopropoxy group rotation in the dissociative mechanism.

When the bond rotates directly without any other conformation change of the catalyst, the energy barrier is 18.3 kcal/mol (**TS0-Dis-1**, **Figure IV-12**). The Ru-C-C-C dihedral angle shown in yellow dash line is 79.8°. The rotation can also occur after an isomerization of the catalyst. In precatalyst **30**, the nitrate ligand is equatorial relative to the NHC ligand. It can isomerize to an axial coordinated conformation and form a five coordinated complex (**CTL0** in **Figure IV-13**). With the assistance of the nitrate ligand isomerization, the rotation barrier of the dissociation

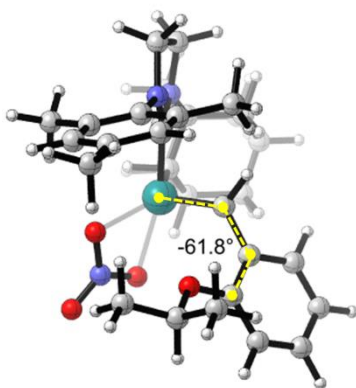


Figure IV-13 Structure isomer of precatalyst **30**.

transition state is only 14.9 kcal/mol (**TS0-Dis-2**, **Figure IV-12**). The Ru-C-C-C dihedral angle in this transition structure is 91.9°.

4.3.1.1.2 Bottom-bound vs. Side-bound Metathesis

After the alkylidene-aryl C-C bond rotation of about 180°, a five-coordinated precatalyst is formed (**Figure IV-14**). **CTL-Dis-1** is formed after only benzylidene ligand rotation. Catalyst

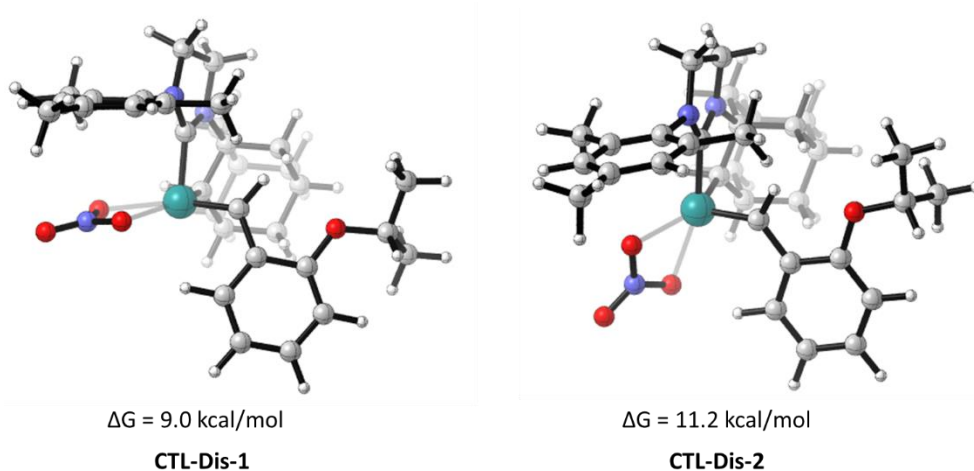


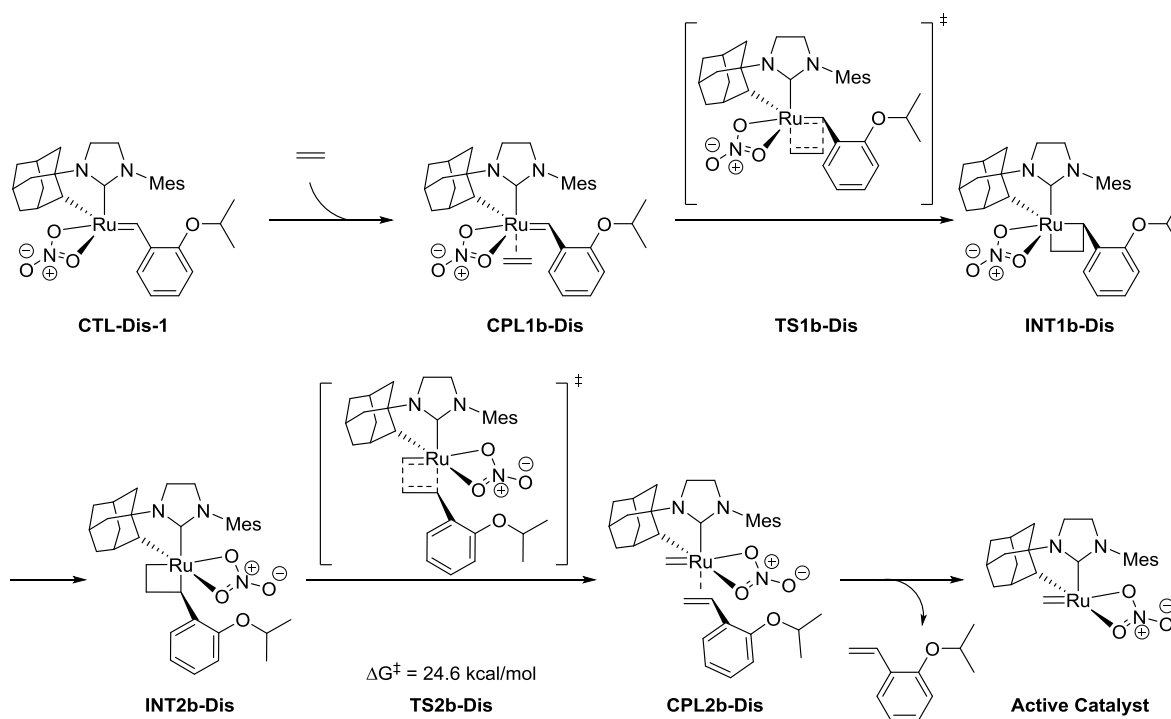
Figure IV-14 The five-coordinated complex is formed after alkylidene-aryl C-C bond rotation.

CTL-Dis-1 is a pentagonal pyramid and a coordinating site is left vacant on the bottom of the ruthenium catalyst. **CTL-Dis-2** is also a trigonal bipyramid with an olefin coordination site on the side position. The free energy of **CTL-Dis-1** is slightly lower than the free energy of **CTL-Dis-2**, and they can interconvert by nitrato rotation.

With a vacant coordination position, the olefin can coordinates with the ruthenium and undergo metathesis to form the active catalyst. Like the mechanism of Z-selective olefin metathesis reaction with active catalyst,⁸¹ there are two possible mechanisms in the metathesis process of the precatalyst. When the olefin substrate coordinates with the ruthenium from the

bottom position, it is called a bottom-bound pathway; when the olefin substrate coordinates with the ruthenium from the side position, it is called a side-bound pathway.

The bottom-bound pathway is shown in **Scheme IV-5**. The olefin substrate coordinates with the catalyst **CTL-Dis-1** from the bottom position and forms complex **CPL1b-Dis**. Through a four-



Scheme IV-5 The bottom-bound pathway in the dissociative mechanism.

membered ring transition state **TS1b-Dis**, the metallacyclobutane intermediate **INT1b-Dis** is formed. Then, the metallocycle isomerizes from the right side to the left side and forms a second intermediate **INT2b-Dis**. The four-membered ring undergoes cycloreversion through **TS2b-Dis**, to form a new complex **CPL2b-Dis**, with the o-isopropoxy styrene then coordinated with ruthenium in the bottom-bound position. Finally, the o-isopropoxy styrene dissociates and form

the active catalyst. The free energy barrier of the cycloreversion is 24.6 kcal/mol separately in the bottom-bound pathway (**Figure IV-15**).

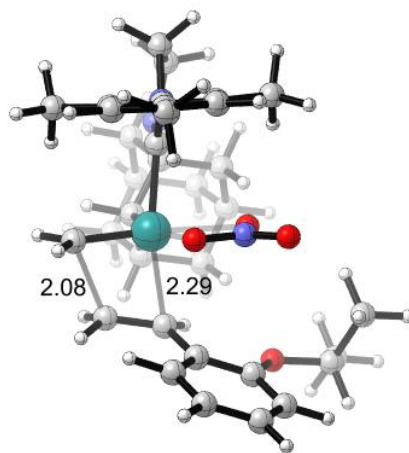
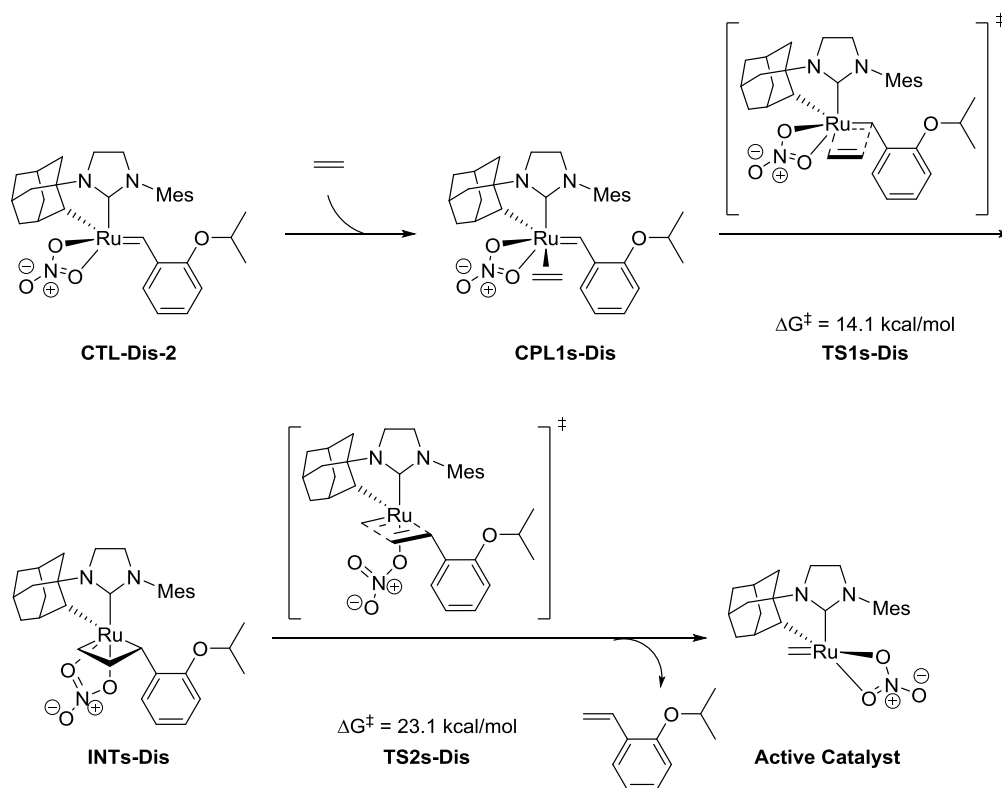


Figure IV-15 Optimized structure of **TS2b-Dis**.



Scheme IV-6 The side-bound pathway in the dissociative mechanism.

The side-bound pathway is shown in **Scheme IV-6**. When the isomerized catalyst **CTL-Dis-2** is formed, the olefin substrate coordinates with ruthenium from the side and forms complex **CPL1s-Dis**. Through a four-membered ring cycloaddition transition state **TS1s-Dis**, the metallacyclobutane intermediate **INTs-Dis** is formed. The bidentate nitrate group becomes partial monodentate in this intermediate and **INTs-Dis** has a trigonal bipyramidal geometry. Different from the bottom-bound pathway, there is no intermediate isomerization to the left side. The metallacyclobutane in **INTs-Dis** undergoes cycloreversion to form the metathesis product. The cycloreversion transition state **TS2s-Dis** is a trigonal bipyramid and the nitrate ligand is monodentate. The activation barriers of the metallacyclobutane formation and cycloreversion are 14.1 kcal/mol and 23.1 kcal/mol separately.

During the initiation, the nitrate ligand can be bidentate or monodentate with the ruthenium. Both the monodentate and bidentate transition states were investigated. It was found that only for **TS2s-Dis**, the monodentate transition structure is favored compared to the bidentate transition structure (**Figure IV-16**). The monodentate transition state structure has lower free energy because

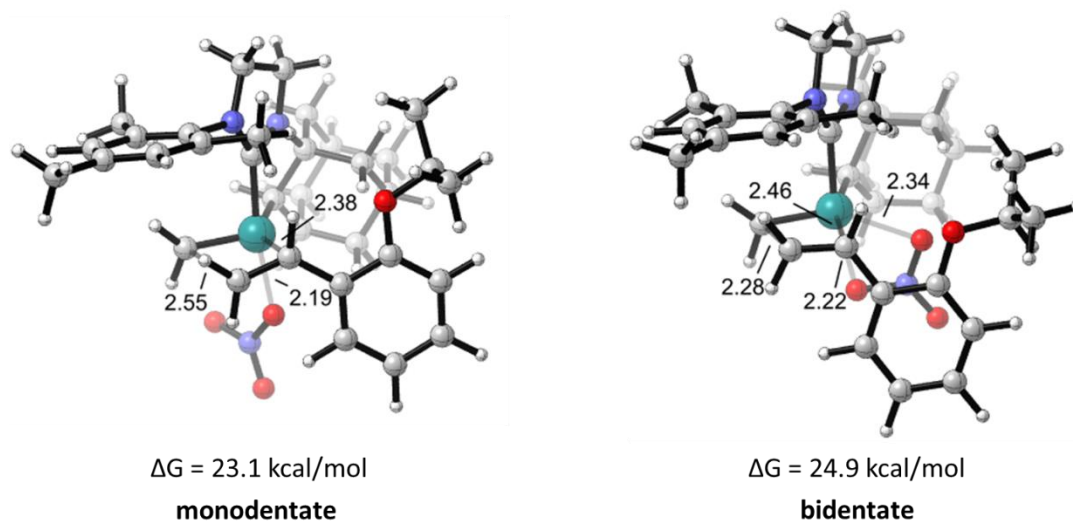


Figure IV-16 The monodentate and bidentate structures of **TS2s-Dis**.

of the steric repulsion caused by the aryl and adamantyl groups in the bidentate transition state

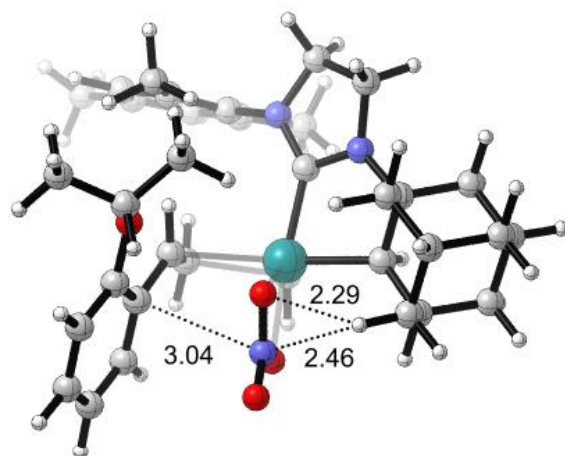


Figure IV-17 Side view of the bidentate structure of **TS2S-Dis**.

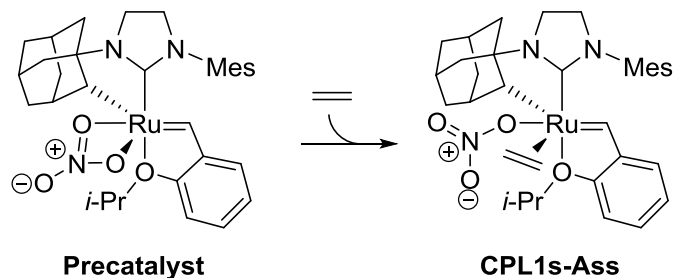
structure (**Figure IV-17**). The distance between the nitrogen of the nitrate ligand and the aryl carbon is only 3.04 Å, which is smaller than the sum of the van der Waals radius of nitrogen and carbon atoms (3.25 Å). Also, the distances of adamantyl hydrogen from the oxygen and nitrogen atoms of nitrate ligand are only 2.29 Å and 2.46 Å respectively.

The free energy barrier of the bottom-bound pathway is 24.6 kcal/mol and the barrier of the side-bound pathway is 23.1 kcal/mol, and the metathesis process of the dissociative mechanism undergoes a side-bound pathway.

4.3.1.2 Associative Mechanism

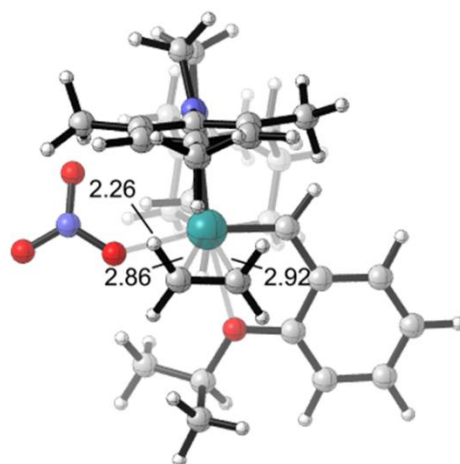
In the associative mechanism, the olefin substrate first coordinates with the ruthenium after the bidentate nitrate ligand becomes monodentate. The ortho-isopropoxy group coordinates with the ruthenium throughout the initiation.

4.3.1.2.1 Association of the Olefin Substrate



Scheme IV-7 Association of the Olefin Substrate from the side position.

The olefin substrate first associates with the ruthenium after the bidentate nitrato ligand becomes monodentate (**Scheme IV-7**). It approaches the ruthenium from the side-bound position and forms a complex **CPL1s-Ass**. The ruthenium of **CPL1s-Ass** is six-coordinated and the



$\Delta G = 12.0$ kcal/mol

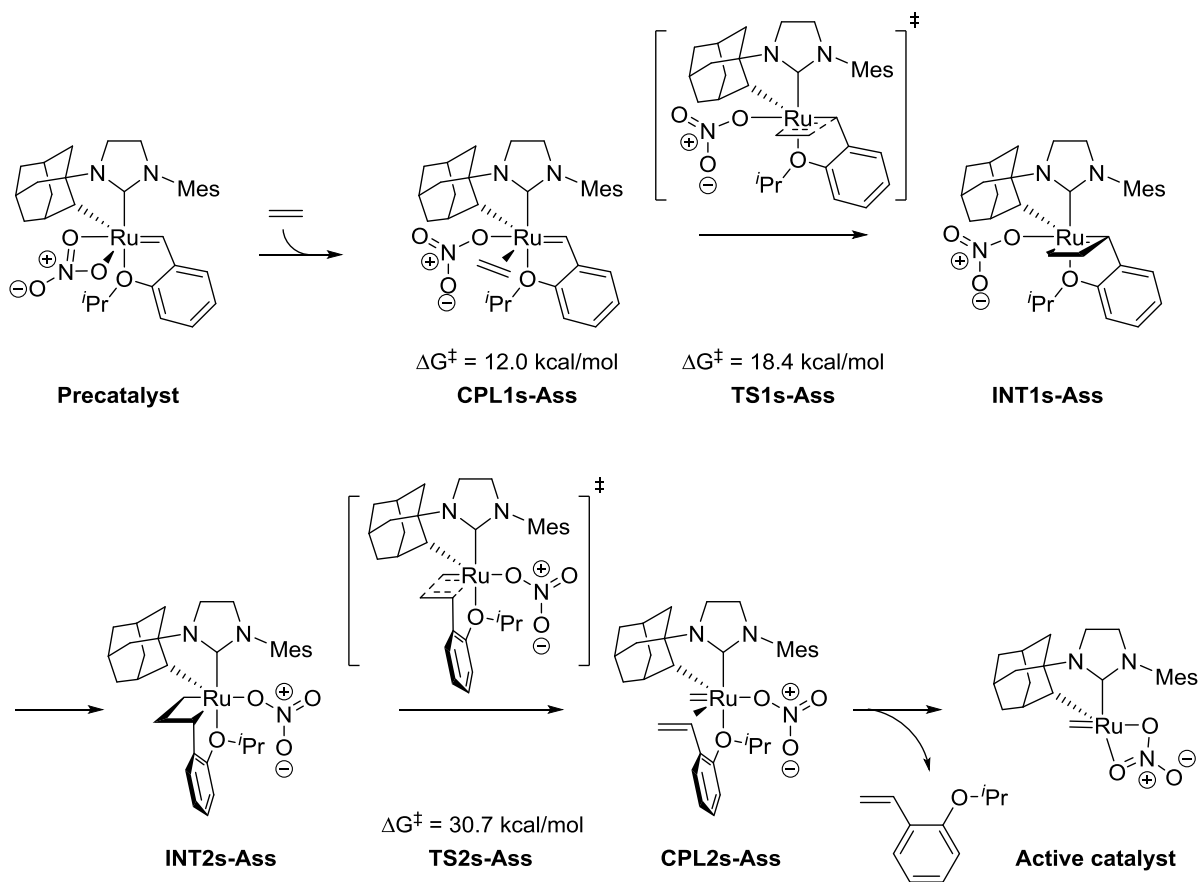
CPL1s-Ass

Figure IV-18 Optimized structure of **CPL1s-Ass**.

geometry of the complex is trigonal bipyramidal (**Figure IV-18**). The free energy of the coordination complex is 12.0 kcal/mol.

4.3.1.2.2 Metathesis Pathway for Initiation by the Associative Mechanism

There are bottom-bound and side-bound pathways for the associative mechanism as well. The side-bound pathway (**Scheme IV-8**) starts from **CPL1s-Ass**. Through a four-membered ring



Scheme IV-8 The side-bound pathway in the associative mechanism.

transition state **TS1s-Ass**, the metallacyclobutane **INT1s-Ass** intermediate is produced. With isomerization, the metallacycle and the nitrate ligand switch position and the ring goes from the right side to the left side of the catalyst and forms **INT2s-Ass**. Then, through another four-membered ring transition state **TS2s-Ass**, the cycloreversion occurs to form complex **CPL2s-Ass**.

The *o*-isopropoxy styrene dissociates from the ruthenium and forms the active catalyst. The free energy barriers of the four-membered ring formation and cycloreversion are 18.4 kcal/mol and 30.7 kcal/mol respectively. The ortho-isopropoxy ligand is always coordinating with the ruthenium in the associative pathway until the active catalyst forms (**Figure IV-19**).

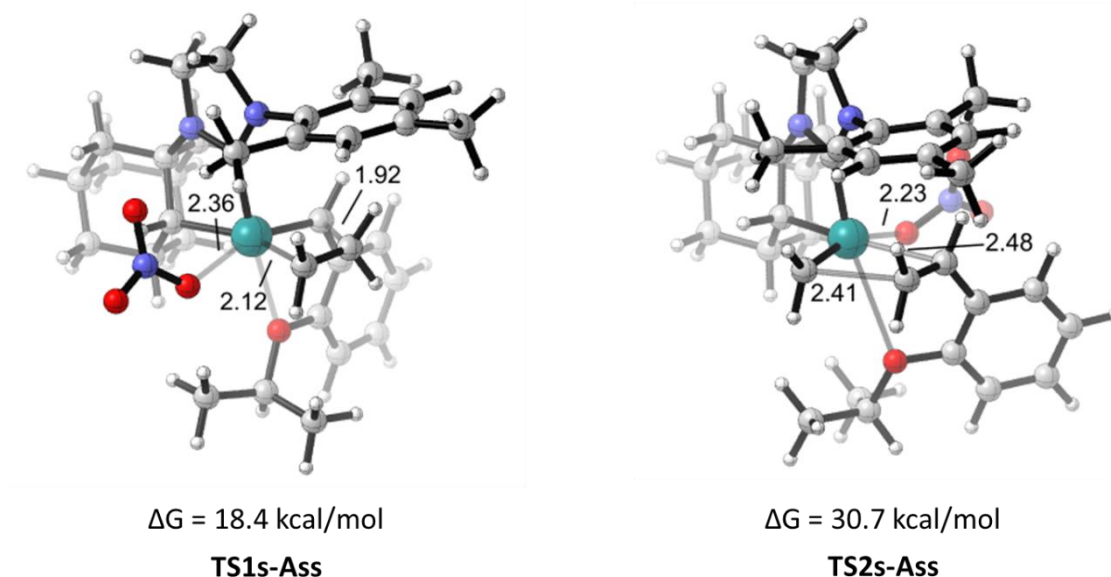
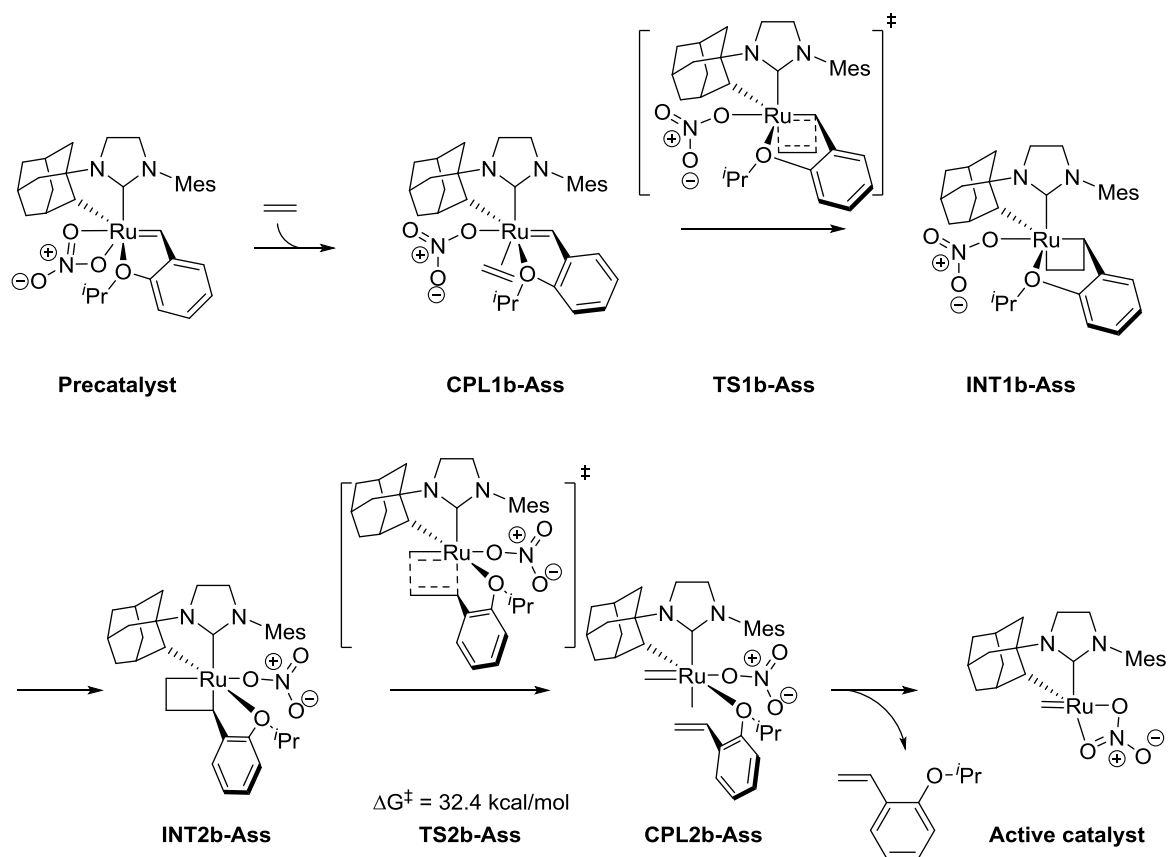


Figure IV-19 Optimized structures of transition states in the associative mechanism.

The bottom-bound pathway was also investigated. In the bottom-bound mechanism, the precatalyst first isomerizes to a different conformation with the ortho-isopropoxyl ligand coordinating with the ruthenium from the side position (**Scheme IV-9**). The nitrate group then become monodentate, and the olefin substrate coordinates with the ruthenium from the bottom. The subsequent steps are similar to the ones in the side-bound pathway, but the ortho-isopropoxy ligand coordinates with the ruthenium from the side and the olefin coordinates with the ruthenium



Scheme IV-9 The bottom-bound pathway in the associative mechanism.

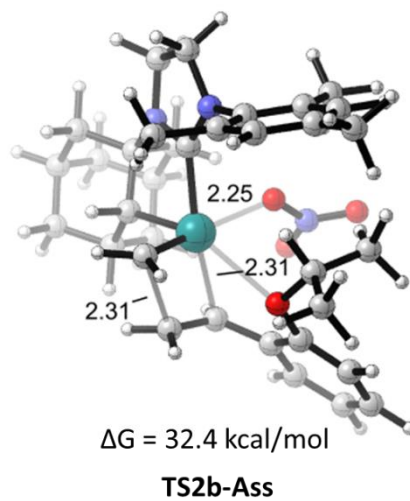


Figure IV-20 Optimized structure of TS2b-Ass.

from the bottom. The free energy barrier of the cycloreversion transition state **TS2b-Ass** (**Figure**

IV-20) is 32.4 kcal/mol, which is 1.7 kcal/mol higher than the barrier of the cycloreversion in the side-bound pathway. The side-bound pathway is favored in the associative mechanism.

4.3.1.3 Summary and the Free Energy Profile

The rate determining steps of both the dissociative and the associative mechanisms are cycloreversion. The free energy barrier of the dissociative mechanism is 23.1 kcal/mol (**TS2s-Dis**), while the barrier of the associative mechanism is 30.7 kcal/mol (**TS2s-Ass**). The dissociative

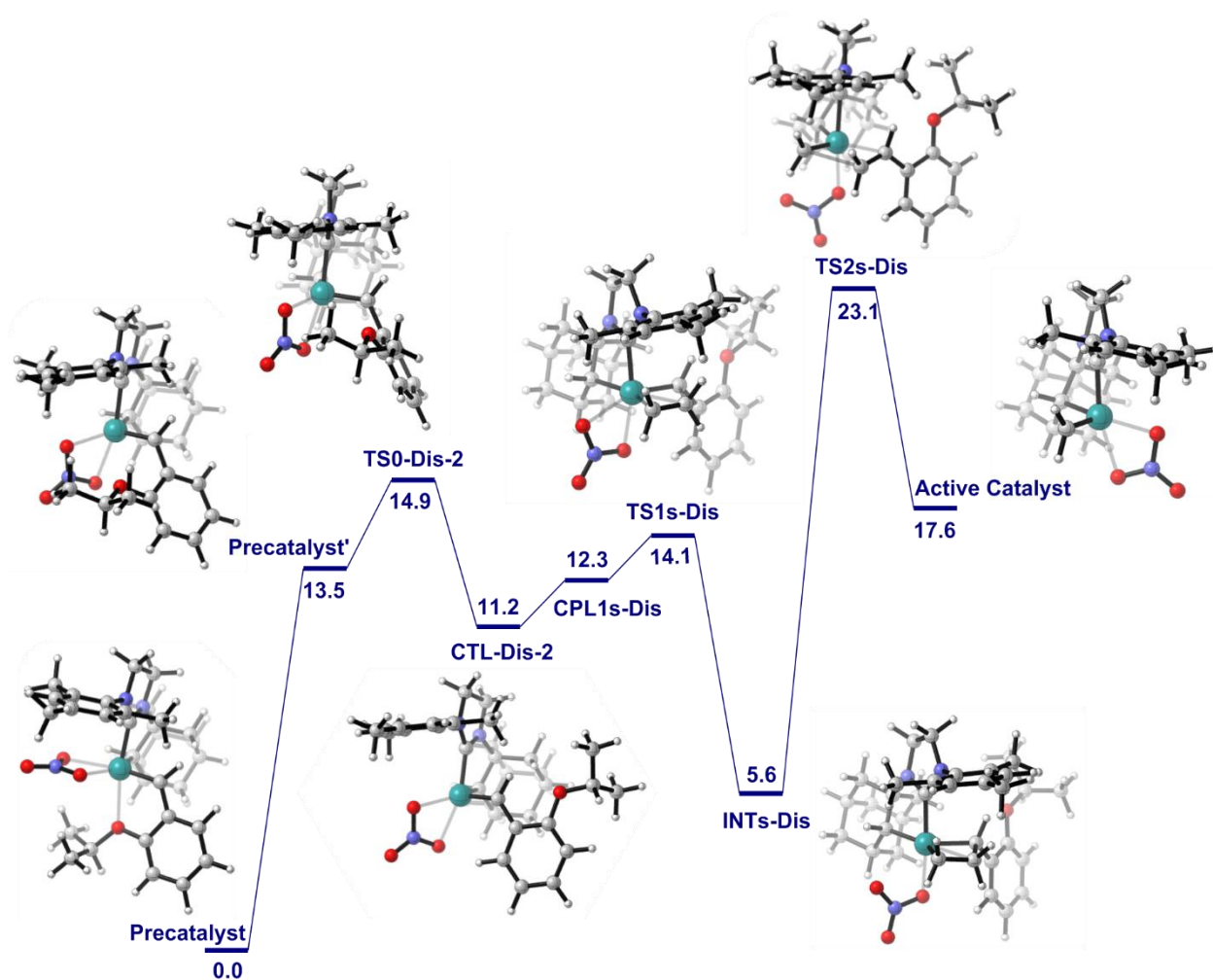


Figure IV-21 Energy profile of the initiation mechanism of the Z-selective Ru catalyst. Free energies are shown in the unit of kcal/mol.

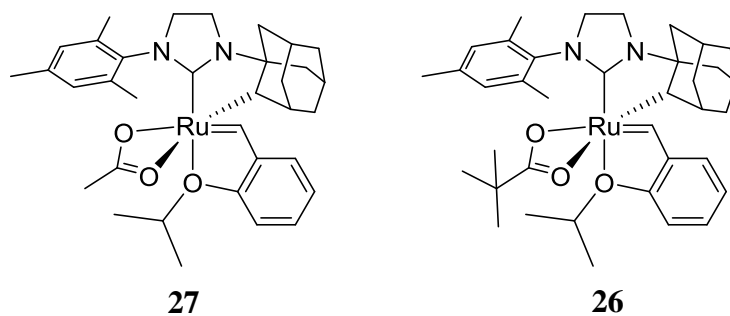
mechanism is favored. Therefore, the initiation of the Z-selective Ru catalyst occurs by a dissociative mechanism. The energy profile of the initiation mechanism is summarized in **Figure IV-21**.

In the initiation of the Z-selective ruthenium catalyst, the nitrate ligand first isomerizes to from the side position to the bottom position (**precatalyst'**). The ortho-isopropoxy ligand then dissociates from the ruthenium through the alkylidene-aryl C-C bond rotation (**TS0-Dis-2**) and forms catalyst structure **CTL-Dis-2**. The free energy barrier of the C-C bond rotation is 14.9 kcal/mol. The free energy of **CTL-Dis-2** is 11.2 kcal/mol relative to the precatalyst. The olefin substrate then coordinates with the ruthenium from the side position and forms complex **CPL1s-Dis**. The free energy of the complex is 12.3 kcal/mol, slightly higher than the overall free energy of **CTL-Dis-2** and olefin substrate. Through a four-membered ring transition state **TS1s-Dis**, the metallacyclobutane intermediate **INTs-Dis** is produced, and the energy barrier is 14.1 kcal/mol. The metallacyclobutane intermediate is quite stable, its free energy is only 5.6 kcal/mol higher than the overall free energy of the precatalyst and the substrate. The ring then undergoes cycloreversion through another four-membered ring transition state **TS2s-Dis** to form the active catalyst. The o-isopropoxy styrene formed directly dissociates from the catalyst after cycloreversion, and there is no reaction complex intermediate formed in this process. The energy barrier of the last step is 23.1 kcal/mol, and the free energy of the product from initiation is 17.6 kcal/mol compared to the precatalyst and ethene. The rate determining step of the initiation is the cycloreversion of the metallacyclobutane intermediate.

4.3.2 Anionic Effects with Initiation Process

4.3.2.1 Steric Effects of the Anionic Ligands

We also investigated the effects of the anionic ligands on the initiation rates. The steric effect was first investigated. The initiation of **27** and **26**, coordinated to an acetate and a pivalate, were studied.



The anionic ligands of catalyst **27** and **26** are both bidentate and their structures are similar. Their initiation mechanisms are the same as discussed in the previous section. Both **27** and **26**

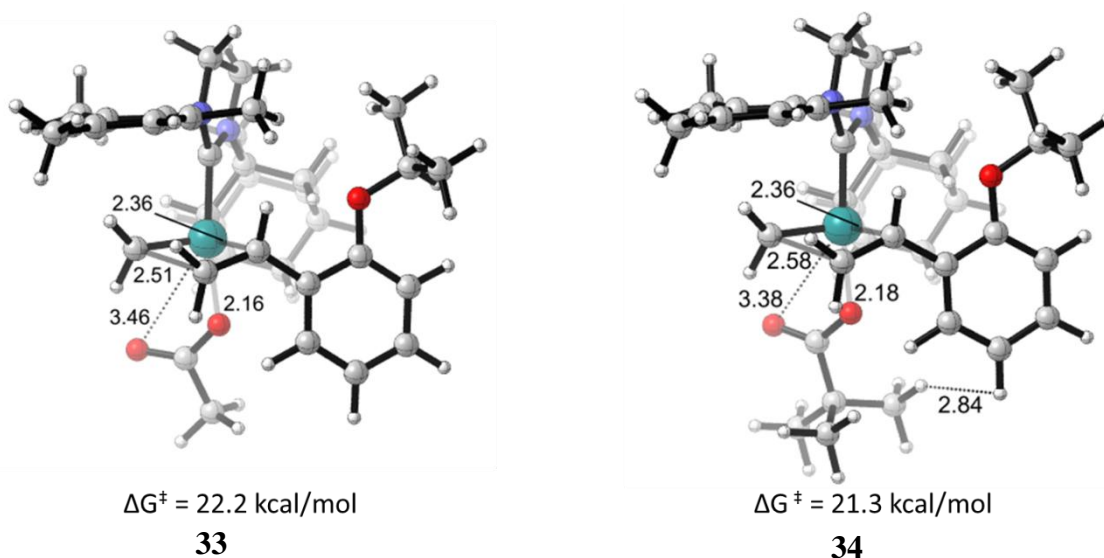


Figure IV-22 The transition state structures of metallacyclobutane cycloreversion of **27** and **26**.

undergo reaction via the dissociative mechanism, and the rate determining steps are the metallacyclobutane cycloreversion (**Figure IV-22**). The initiation free energy barriers of **27** and **26** are 21.3 kcal/mol and 22.2 kcal/mol, respectively.

The computational results agree with the experiment, where the initiation rate of **26** is about five times the rate of **27** (**Table IV-1**).

The initiation of **26** is faster because of the steric effects of the pivalate ligands. There are steric repulsions between the precatalyst hydrogens and the isopropyl group on the Hoveyda ligand (**Figure IV-23**).

In catalyst **27**, the distances between the acetate ligand and other substituents are large and the dihedral angle of C₁-C₂-C₃-Ru is 85.4°. The NHC ring is puckered and the torsional strain is

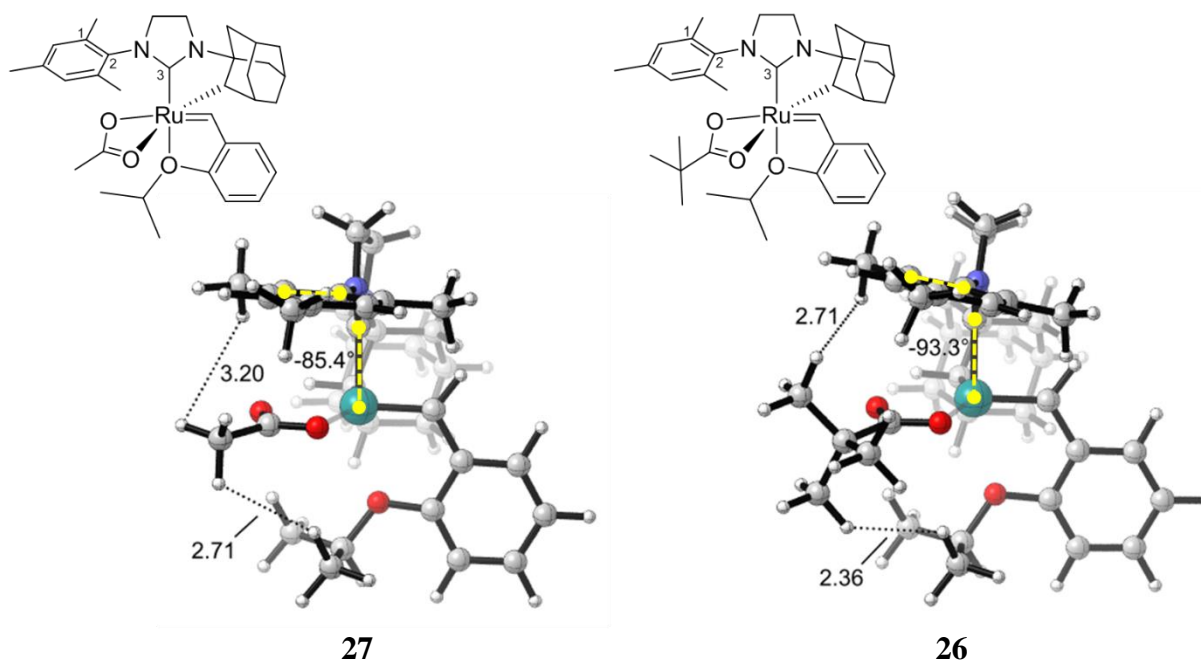


Figure IV-23 Steric repulsions exist in the precatalyst **26**.

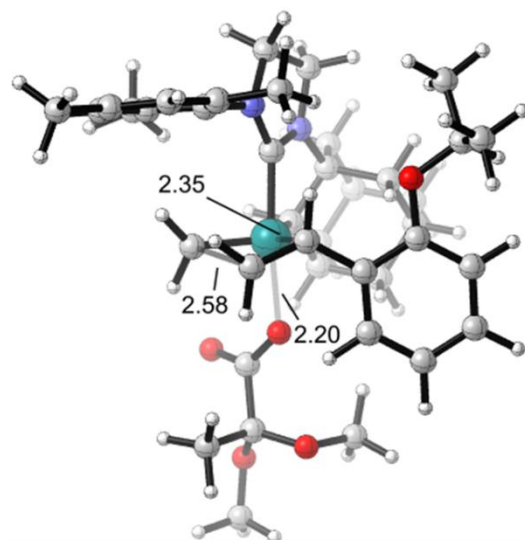
negligible. However, in catalyst **26**, the distance between the methyl hydrogen of pivalate and the

isopropyl hydrogen is 2.36 Å, slightly smaller than the van der Waals radius. The dihedral angle of C₁-C₂-C₃-Ru is 93.3° much bigger than the angle in **27**.

In the transition state structures, the steric strain is released. The ortho-isopropoxyl group rotates away from the anionic ligand and the anionic ligand becomes monodentate (**Figure IV-22**). Both the NHC rings in **33** and **34** are puckered and their geometries are similar.

4.3.2.2 Electronic Effects of the Anionic Ligands

The electronic effects was studied with catalyst **29**. The initiation mechanism of **29** is the same as **30** and the initiation barrier depends on the free energy of the metallacyclobutane cycloreversion transition state. The structure of the rate determining transition state **35** was optimized and shown below in **Figure IV-25**. The free energy of **35** is 19.8 kcal/mol, which is 0.5 kcal/mol lower than the free energy of **34**. This agrees with the experimental result that the initiation rate of **29** slightly higher than the initiation rate of **26** (**Table IV-1**).



$$\Delta G^\ddagger = 19.8 \text{ kcal/mol}$$

35

Figure IV-25 Optimized transition state structure of the metallacyclobutane cycloreversion.

The initiation of **29** is faster than the rate of **26** because the oxygen groups in the anionic ligand makes the ligand less nucleophilic and the coordination weaker. The Ru-O distances are 2.48 Å and 2.25 Å separately (**Figure IV-24**), one of which slightly longer than the Ru-O distance

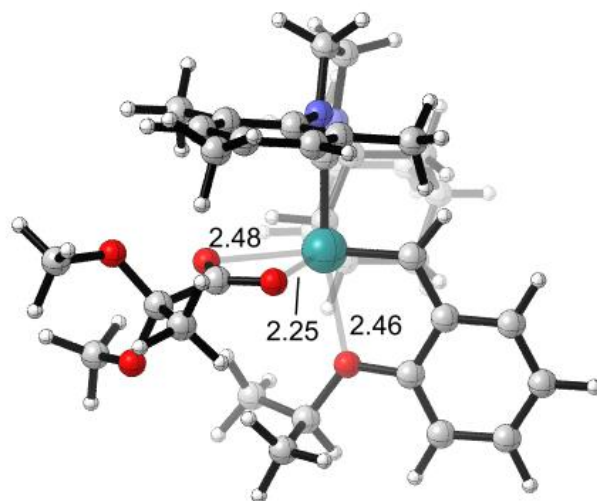


Figure IV-24 Optimized structure of **29**.

75

in **26** (2.45 Å), indicating less coordination between O and Ru. The weaker coordination of the anionic ligand makes it favor a monodentate structure (**35**).

4.3.2.3 Initiation Mechanism of the Monodentate Ruthenium Catalysts

To explore the effect of the coordination number of anionic ligands on the initiation, the initiation mechanism of monodentate catalyst **31** was investigated. The structure of **31** is shown

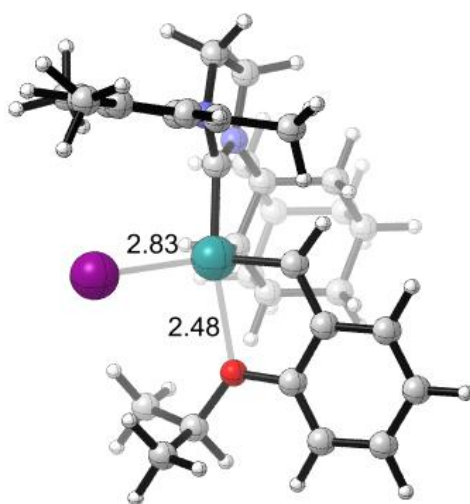
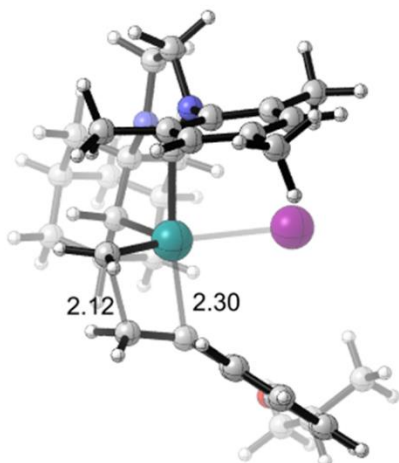


Figure IV-26 Optimized structure of **31**.

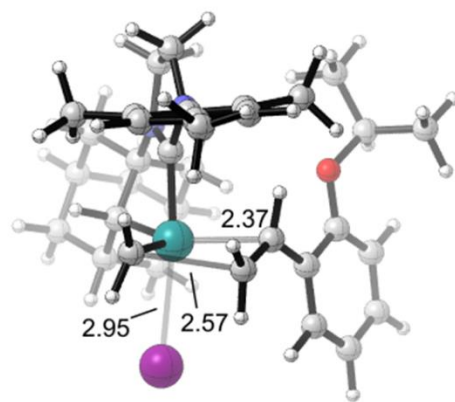
in **Figure IV-26**. The iodo ligand coordinates with ruthenium from the side position, and the geometry of the precatalyst is trigonal bipyramidal.

Similar to the initiation mechanism exploration for catalyst **30**, there are four possible mechanisms for **31**: dissociative-bottom, dissociative-side, associative-bottom and associative-side. The transition state structures and their free energies of the rate determining steps in the four possible pathways are shown below (**Figure IV-27**).



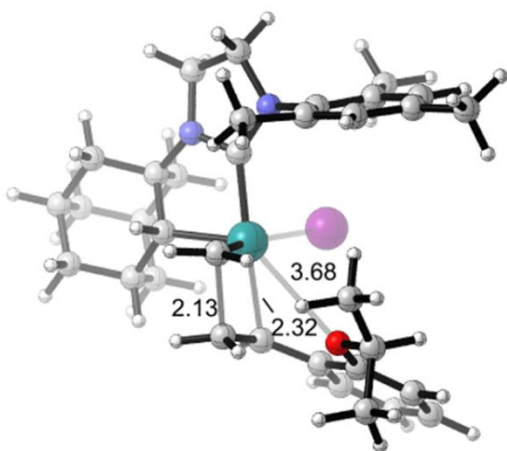
$$\Delta G^\ddagger = 26.0 \text{ kcal/mol}$$

Dissociative-Bottom



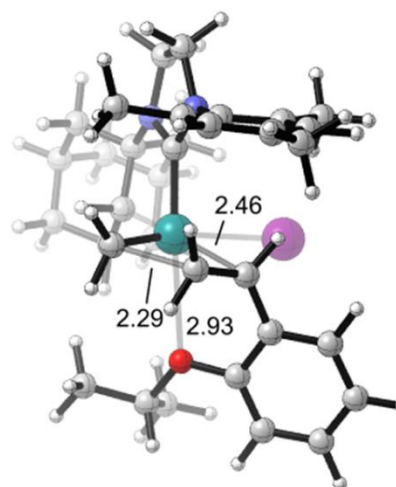
$$\Delta G^\ddagger = 22.2 \text{ kcal/mol}$$

Dissociative-Side



$$\Delta G^\ddagger = 28.4 \text{ kcal/mol}$$

Associative-Bottom



$$\Delta G^\ddagger = 34.5 \text{ kcal/mol}$$

Associative-Side

Figure IV-27 Rate determining transition state structures of the four possible initiation pathways of **31**.

Among all the four possible pathways, the energy barrier of the dissociative-side pathway is the lowest (22.2 kcal/mol) and the iodo ligated catalyst **31** undergoes a dissociative initiation mechanism with the olefin substrate side-bounded to the ruthenium.

The initiation mechanism of precatalyst **31** is quite similar to the mechanism of **30**. The ortho-isopropoxy ligand first dissociates from the ruthenium with rotation of alkylidene-aryl C-C bond (**Figure IV-28**).

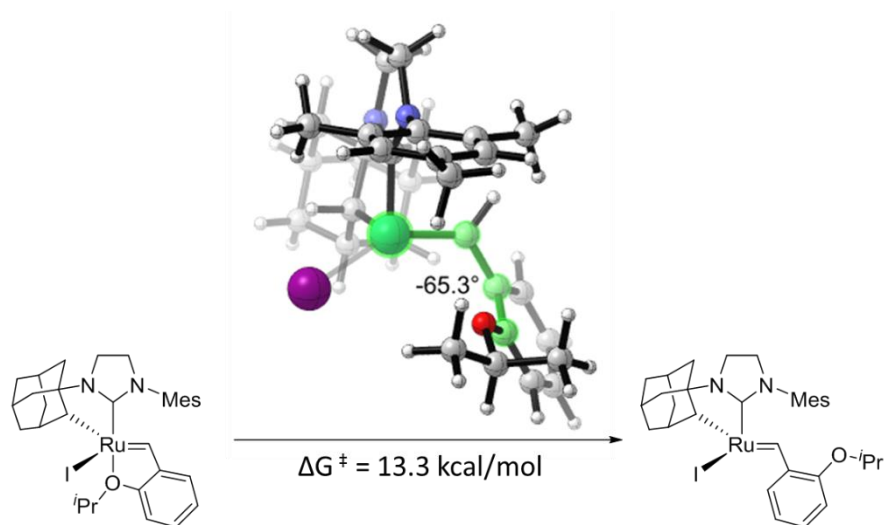


Figure IV-28 The first step in the dissociative initiation of **31**.

The olefin substrate then coordinates with the ruthenium from the side-bound position and undergoes metathesis with the side-bound pathway (**Figure IV-29**). The free energy barriers of

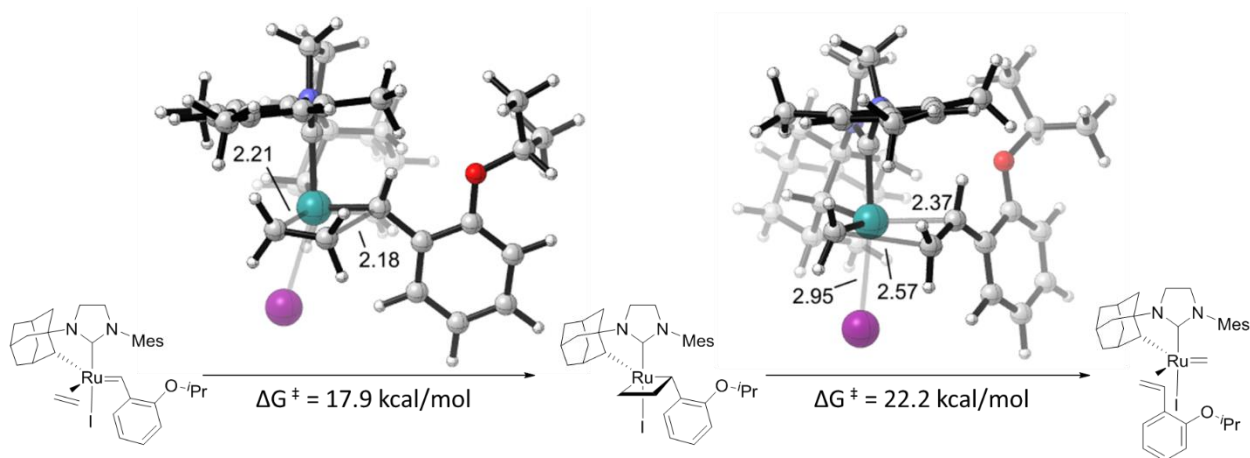


Figure IV-29 Metathesis steps in the initiation of **31**.

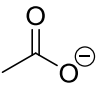
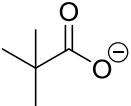
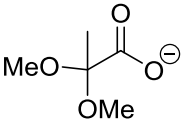
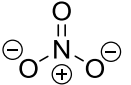

the metallacyclobutane formation and cyclereversion are 17.9 kcal/mol and 22.2 kcal/mol separately. The overall barrier of the initiation of **31** is 22.2 kcal/mol.

4.3.2.4 Summary of Anionic Effects

The activation barriers for the initiation with different anionic ligands are summarized in

Table IV-2.

Table IV-2 The experimental initiation rates and computational activation barriers with different anionic ligands.

Catalyst Number	Anionic ligand	Temp, °C	Initiation rate constant, 10 ⁻³ s ⁻¹	ΔG [‡] , kcal/mol
27	 acetate	30	0.17 ± 0.04	22.2
26	 pivalate	30	0.87 ± 0.02	21.3
29	 2,2-dimethoxypropionate	30	2.5 ± 0.1	19.8
30	 nitrate	30	0.84 ± 0.03	23.1
31	 iodo	50	0.17 ± 0.01	22.2

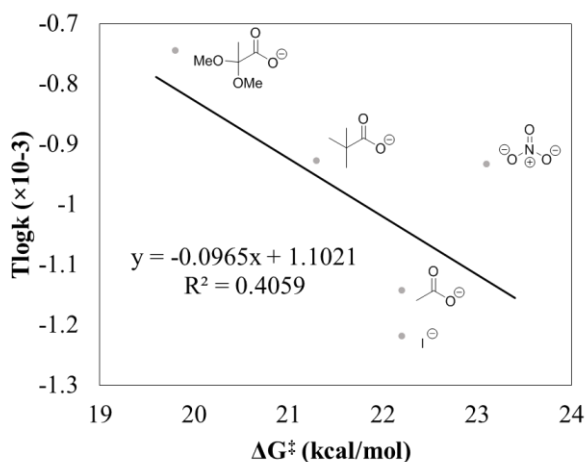


Figure IV-30 Correlation of experimental rate constant and computational free energy barrier of chelated Ru catalysts with different anionic ligands.

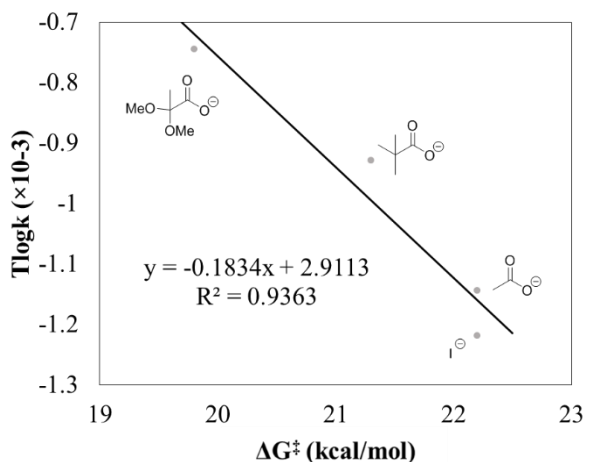


Figure IV-31 Correlation of experimental rate constant and computational free energy barrier of chelated Ru catalysts with different anionic ligands (excluding nitrato ligated catalyst).

With the plot of the log value of the experimental rate constant versus the computed activation free energy barrier of the initiation (**Figure IV-30** and **Figure IV-31**), it can be concluded that the computational activation barrier trend for the catalysts with acetate, pivalate and 2,2-dimethoxypropionate agrees well with the experimental initiation rates as discussed above. The ligand size and electronegativity influences the initiation rate by controlling the relative stabilities of the precatalysts.

However, the computational results for the nitrato ligated and iodo ligated catalysts shows difference from the experimental results. Catalyst **30** which coordinates with nitrato ligand has a large initiation rate constant comparable to catalyst **26**. However, the computed activation barrier of **30** is 1.8 kcal/mol higher than **26**. The iodo coordinated catalyst **31** has the slowest initiation rate among the five catalysts but the computed activation barrier is equal to the barrier of **27**. These disagreements might come from the computational methods. Alternatively, other factors such as catalyst decomposition should be considered.

4.4 CONCLUSION

The chelated Z-selective ruthenium catalysts undergoes initiation processes by a dissociative mechanism. The rate determining step of initiation is the metallacyclobutane cycloreversion. The activation barrier of the initiation is around 20 kcal/mol, and the initiation is slower than the olefin metathesis with active catalysts.

The size and the electronegativity of the anionic ligands influences the initiation rate. The larger the anionic ligands are, the faster the initiations. Anionic ligands with high electronegativity can also accelerate the initiation.

Current computational results cannot explain the difference between the monodentate and bidentate ligands. Other reactions like catalyst decomposition will be considered in the future.

References

- (1) Hohenberg, P.; Kohn, W. *Phys. Rev.* **1964**, *136* (3B), B864–B871.
- (2) Kohn, W.; Sham, L. J. *Phys. Rev.* **1965**, *140* (4A).
- (3) Becke, A. D. *J. Chem. Phys.* **1993**, *98* (2).
- (4) Lee, C.; Yang, W.; Parr, R. G. *Phys. Rev. B* **1988**, *37* (2), 785–789.
- (5) Grimme, S. *Wiley Interdiscip. Rev. Comput. Mol. Sci.* **2011**, *1* (2), 211–228.
- (6) Grimme, S.; Antony, J.; Ehrlich, S.; Krieg, H. *J. Chem. Phys.* **2010**, *132* (15).
- (7) Peverati, R.; Truhlar, D. G. **2012**.
- (8) Zhao, Y.; Truhlar, D. G. *J. Phys. Chem. A* **2006**, *110* (15), 5121–5129.
- (9) Hehre, W. J.; Ditchfield, R.; Pople, J. A. *J. Chem. Phys.* **1972**, *56* (5).
- (10) Schwerdtfeger, P.; Dolg, M.; Schwarz, W. H. E.; Bowmaker, G. A.; Boyd, P. D. W. *J. Chem. Phys.* **1989**, *91* (3).
- (11) Hay, P. J.; Wadt, W. R. *J. Chem. Phys.* **1985**, *82* (1), 270.
- (12) Hay, P. J.; Wadt, W. R. *J. Chem. Phys.* **1985**, *82* (1), 284.
- (13) Head-Gordon, M.; Pople, J. A. *J. Chem. Phys.* **1988**, *89* (9), 299.
- (14) Nicklass, A.; Dolg, M.; Stoll, H.; Preuss, H. *J. Chem. Phys.* **1995**, *102* (22), 8942.
- (15) (a) Miertuš, S.; Scrocco, E.; Tomasi, J. *Chem. Phys.* **1981**, *55* (1), 117–129. (b) Miertuš, S.; Tomasi, J. *Chem. Phys.* **1982**, *65* (2), 239–245. (c) Pascual-ahuir, J. L.; Silla, E.; Tuñon, I. *J. Comput. Chem.* **1994**, *15* (10), 1127–1138.
- (16) Barone, V.; Cossi, M. *J. Phys. Chem. A* **1998**, *102* (11), 1995–2001. (b) Cossi, M.; Rega, N.; Scalmani, G.; Barone, V. *J. Comput. Chem.* **2003**, *24* (6), 669–681.
- (17) Klamt, A.; Schuurmann, G. *J. Chem. Soc., Perkin Trans. 2* **1993**, No. 5, 799–805.

- (18) Marenich, A. V.; Cramer, C. J.; Truhlar, D. G. *J. Phys. Chem. B* **2009**, *113* (18), 6378–6396.
- (19) Fukui, K. *Acc. Chem. Res.* **1981**, *14* (12), 363–368.
- (20) Fukui, K. *J. Phys. Chem.* **1970**, *74* (23), 4161–4163.
- (21) Gaussian 09, Revision D.01, Frisch, M. J.; Trucks, G. W.; Schlegel, H. B.; Scuseria, G. E.; Robb, M. A.; Cheeseman, J. R.; Scalmani, G.; Barone, V.; Mennucci, B.; Petersson, G. A.; Nakatsuji, H.; Caricato, M.; Li, X.; Hratchian, H. P.; Izmaylov, A. F.; Bloino, J.; Zheng, G.; Sonnenberg, J. L.; Hada, M.; Ehara, M.; Toyota, K.; Fukuda, R.; Hasegawa, J.; Ishida, M.; Nakajima, T.; Honda, Y.; Kitao, O.; Nakai, H.; Vreven, T.; Montgomery, J. A., Jr.; Peralta, J. E.; Ogliaro, F.; Bearpark, M.; Heyd, J. J.; Brothers, E.; Kudin, K. N.; Staroverov, V. N.; Kobayashi, R.; Normand, J.; Raghavachari, K.; Rendell, A.; Burant, J. C.; Iyengar, S. S.; Tomasi, J.; Cossi, M.; Rega, N.; Millam, J. M.; Klene, M.; Knox, J. E.; Cross, J. B.; Bakken, V.; Adamo, C.; Jaramillo, J.; Gomperts, R.; Stratmann, R. E.; Yazyev, O.; Austin, A. J.; Cammi, R.; Pomelli, C.; Ochterski, J. W.; Martin, R. L.; Morokuma, K.; Zakrzewski, V. G.; Voth, G. A.; Salvador, P.; Dannenberg, J. J.; Dapprich, S.; Daniels, A. D.; Farkas, Ö.; Foresman, J. B.; Ortiz, J. V.; Cioslowski, J.; Fox, D. J. Gaussian, Inc., Wallingford CT, 2009.
- (22) **Schrödinger Release 2014-2**: Maestro, version 9.8, Schrödinger, LLC, New York, NY, 2014.
- (23) Slomkowski, S.; Penczek, S.; Duda, A. *Polym. Adv. Technol.* **2014**, *2014* (February).
- (24) Dechy-Cabaret, O.; Martin-Vaca, B.; Bourissou, D. *Chem. Rev.* **2004**, *104* (12), 6147–6176.
- (25) Kleine, V. J.; Kleine, H.-H. *Die Makromol. Chemie* **1959**, *30* (1), 23–38.

- (26) (a) Dittrich, V. W.; Schulz, R. C. *Die Angew. Makromol. Chemie* **1971**, *15* (1), 109–126. (b) Kricheldorf, H. R.; Berl, M.; Scharnagl, N. *Macromolecules* **1988**, *21* (2), 286–293. (c) Dubois, P.; Jacobs, C.; Jerome, R.; Teyssie, P. *Macromolecules* **1991**, *24* (9), 2266–2270. (d) Degée, P.; Dubois, P.; Jérôme, R. *Macromol. Symp.* **1997**, *123* (1), 67–84; *Macromol. Chem. Phys.* **1997**, *198* (6), 1973–1984. (e) Eguiburu, J. L.; Fernandez-Berridi, M. J.; Cossío, F. P.; Román, J. S. *Macromolecules* **1999**, *32* (25), 8252–8258. (f) von Schenck, H.; Ryner, M.; Albertsson, A.-C.; Svensson, M. *Macromolecules* **2002**, *35* (h), 1556–1562.
- (27) Spassky, N.; Wisniewski, M.; Pluta, C.; Le Borgne, A. *Macromol. Chem. Phys.* **1996**, *197* (9), 2627–2637.
- (28) Spassky, N. *Ring-Opening Polymerisation.*; Rapra Technology Ltd: Shawbury, Shrewsbury, Shropshire, UK, 1995.
- (29) Nomura, N.; Ishii, R.; Akakura, M.; Aoi, K. *J. Am. Chem. Soc.* **2002**, *124* (21), 5938–5939.
- (30) (a) Bakewell, C.; Cao, T.-P.-A.; Long, N.; Le Goff, X. F.; Auffrant, A.; Williams, C. K. *J. Am. Chem. Soc.* **2012**, *134* (51), 20577–20580. (b) Bakewell, C.; White, A. J. P.; Long, N. J.; Williams, C. K. *Angew. Chemie Int. Ed.* **2014**, *53* (35), 9226–9230. (c) Bakewell, C.; White, A. J. P.; Long, N. J.; Williams, C. K. *Inorg. Chem.* **2015**, *54*, 2204–2212.
- (31) Mou, Z.; Liu, B.; Wang, M.; Xie, H.; Li, P.; Li, L.; Li, S.; Cui, D. *Chem. Commun.* **2014**, *50* (77), 11411–11414.
- (32) Kamber, N. E.; Jeong, W.; Waymouth, R. M.; Pratt, R. C.; Lohmeijer, B. G. G.; Hedrick, J. L. *Chem. Rev.* **2007**, *107* (12), 5813–5840.
- (33) Bourissou, D.; Moebs-Sanchez, S.; Martín-Vaca, B. *Comptes Rendus Chim.* **2007**, *10* (9), 775–794.

- (34) Nederberg, F.; Connor, E. F.; Möller, M.; Glauser, T.; Hedrick, J. L. *Angew. Chemie Int. Ed.* **2001**, *40* (14), 2712–2715. (2) Nederberg, F.; Connor, E. F.; Glauser, T.; Hedrick, J. L. *Chem. Commun.* **2001**, No. 20, 2066–2067.
- (35) Lohmeijer, B. G. G.; Pratt, R. C.; Leibfarth, F.; Logan, J. W.; Long, D. A.; Dove, A. P.; Nederberg, F.; Choi, J.; Wade, C.; Waymouth, R. M.; Hedrick, J. L. *Macromolecules* **2006**, *39* (25), 8574–8583.
- (36) Pratt, R. C.; Lohmeijer, B. G. G.; Long, D. A.; Waymouth, R. M.; Hedrick, J. L. *J. Am. Chem. Soc.* **2006**, *128* (14), 4556–4557.
- (37) Dove, A. P.; Pratt, R. C.; Lohmeijer, B. G. G.; Waymouth, R. M.; Hedrick, J. L. *J. Am. Chem. Soc.* **2005**, *127* (40), 13798–13799.
- (38) Myers, M.; Connor, E. F.; Glauser, T.; Möck, A.; Nyce, G.; Hedrick, J. L. *J. Polym. Sci. Part A Polym. Chem.* **2002**, *40* (7), 844–851.
- (39) Coulembier, O.; Lohmeijer, B. G. G.; Dove, A. P.; Pratt, R. C.; Mespouille, L.; Culkin, D. A.; Benight, S. J.; Dubois, P.; Waymouth, R. M.; Hedrick, J. L. *Macromolecules* **2006**, *39* (17), 5617–5628.
- (40) Fevre, M.; Pinaud, J.; Gnanou, Y.; Vignolle, J.; Taton, D. *Chem. Soc. Rev.* **2013**, *42* (5), 2142–2172.
- (41) Kamber, N. E.; Jeong, W.; Waymouth, R. M.; Pratt, R. C.; Lohmeijer, B. G. G.; Hedrick, J. L. *Chem. Rev.* **2007**, *107* (12), 5813–5840.
- (42) Kiesewetter, M. K.; Shin, E. J.; Hedrick, J. L.; Waymouth, R. M. *Macromolecules* **2010**, *43* (5), 2093–2107.
- (43) Williams, K. A.; Neilson, B. M.; Bielawski, C. W. In *Materials Science and Technology*; Wiley-VCH Verlag GmbH & Co. KGaA, 2006.

- (44) Teator, A. J.; Lastovickova, D. N.; Bielawski, C. W. *Chem. Rev.* **2016**, *116* (4), 1969–1992.
- (45) Connor, E. F.; Nyce, G. W.; Myers, M.; Möck, A.; Hedrick, J. L. *J. Am. Chem. Soc.* **2002**, *124* (6), 914–915.
- (46) Fevre, M.; Pinaud, J.; Gnanou, Y.; Vignolle, J.; Taton, D. *Chem. Soc. Rev.* **2013**, *42* (5), 2142–2172.
- (47) Kieseewetter, M. K.; Shin, E. J.; Hedrick, J. L.; Waymouth, R. M. *Macromolecules* **2010**, *43* (5), 2093–2107.
- (48) Neilson, B. M.; Bielawski, C. W. *Chem. Commun.* **2013**, *49* (48), 5453–5455.
- (49) Neilson, B. M.; Bielawski, C. W. *J. Am. Chem. Soc.* **2012**, *134* (30), 12693–12699.
- (50) Jensen, T. R.; Breyfogle, L. E.; Hillmyer, M. A.; Tolman, W. B. *Chem. Commun.* **2004**, No. 21, 2504–2505.
- (51) Dove, A. P.; Li, H.; Pratt, R. C.; Lohmeijer, B. G. G.; Culkin, D. A.; Waymouth, R. M.; Hedrick, J. L. *Chem. Commun.* **2006**, No. 27, 2881–2883.
- (52) Lai, C.-L.; Lee, H. M.; Hu, C.-H. *Tetrahedron Lett.* **2005**, *46* (37), 6265–6270.
- (53) Bonduelle, C.; Martín-Vaca, B.; Cossío, F. P.; Bourissou, D. *Chem. – A Eur. J.* **2008**, *14* (17), 5304–5312.
- (54) Chuma, A.; Horn, H. W.; Swope, W. C.; Pratt, R. C.; Zhang, L.; Lohmeijer, B. G. G.; Wade, C. G.; Waymouth, R. M.; Hedrick, J. L.; Rice, J. E. *J. Am. Chem. Soc.* **2008**, *130* (21), 6749–6754.
- (55) Acharya, A. K.; Chang, Y. A.; Jones, G. O.; Rice, J. E.; Hedrick, J. L.; Horn, H. W.; Waymouth, R. M. *J. Phys. Chem. B* **2014**, *118* (24), 6553–6560.

- (56) Jones, G. O.; Chang, Y. A.; Horn, H. W.; Acharya, A. K.; Rice, J. E.; Hedrick, J. L.; Waymouth, R. M. *J. Phys. Chem. B* **2015**, *119* (17), 5728–5737.
- (57) Wang, Y.; Zhang, L.; Guo, X.; Zhang, R.; Li, J. *J. Polym. Res.* **2013**, *20* (3), 1–6.
- (58) Nobel Media AB. *Nobelprize.org* **2014**, *1* (7), 1–7.
- (59) Ma, S. *Modern Organic Synthesis Reactions Involving Metal*; Guangzhou Science and Technology Press: Guangzhou, **2001**; p 156.
- (60) (a) Murdzek, J. S.; Schrock, R. R. *Organometallics* **1987**, *6* (6), 1373–1374. (b) Schrock, R. R.; Krouse, S. A.; Knoll, K.; Feldman, J.; Murdzek, J. S.; Yang, D. C. *J. Mol. Catal.* **1988**, *46* (1), 243–253. (c) Schrock, R. R.; Murdzek, J. S.; Bazan, G. C.; Robbins, J.; DiMare, M.; O'Regan, M. *J. Am. Chem. Soc.* **1990**, *112* (10), 3875–3886. (d) Bazan, G. C.; Oskam, J. H.; Cho, H. N.; Park, L. Y.; Schrock, R. R. *J. Am. Chem. Soc.* **1991**, *113* (18), 6899–6907.
- (61) Nguyen, S. T.; Johnson, L. K.; Grubbs, R. H.; Ziller, J. W. *J. Am. Chem. Soc.* **1992**, *114* (10), 3974–3975.
- (62) (a) Schwab, P.; France, M. B.; Ziller, J. W.; Grubbs, R. H. *Angew. Chemie Int. Ed. English* **1995**, *34* (18), 2039–2041. (b) Schwab, P.; France, M. B.; Ziller, J. W.; Grubbs, R. H. *Angew. Chemie* **1995**, *107* (18), 2179–2181.
- (63) Schwab, P.; Grubbs, R. H.; Ziller, J. W. *J. Am. Chem. Soc.* **1996**, *118* (1), 100–110.
- (64) Kingsbury, J. S.; Harrity, J. P. A.; Bonitatebus, P. J.; Hoveyda, A. H. *J. Am. Chem. Soc.* **1999**, *121* (4), 791–799.
- (65) Garber, S. B.; Kingsbury, J. S.; Gray, B. L.; Hoveyda, A. H. *J. Am. Chem. Soc.* **2000**, *122* (34), 8168–8179.
- (66) Pederson, R. L.; Fellows, I. M.; Ung, T. A.; Ishihara, H.; Hajela, S. P. *Adv. Synth. Catal.* **2002**, *344* (6-7), 728–735.

- (67) Flook, M. M.; Jiang, A. J.; Schrock, R. R.; Hoveyda, A. H. *J. Am. Chem. Soc.* 2009, 131 (23), 7962–7963.
- (68) (a) Hock, A. S.; Schrock, R. R.; Hoveyda, A. H. *J. Am. Chem. Soc.* 2006, 128 (50), 16373–16375. (b) Singh, R.; Schrock, R. R.; Müller, P.; Hoveyda, A. H. *J. Am. Chem. Soc.* 2007, 129 (42), 12654–12655.
- (69) Jiang, A. J.; Zhao, Y.; Schrock, R. R.; Hoveyda, A. H. *J. Am. Chem. Soc.* 2009, 131 (46), 16630–16631.
- (70) Meek, S. J.; O'Brien, R. V.; Llaveria, J.; Schrock, R. R.; Hoveyda, A. H. *Nature* 2011, 471 (7339), 461–466.
- (71) (a) Marinescu, S. C.; Schrock, R. R.; Müller, P.; Takase, M. K.; Hoveyda, A. H. *Organometallics* 2011, 30 (7), 1780–1782. (b) Peryshkov, D. V.; Schrock, R. R.; Takase, M. K.; Müller, P.; Hoveyda, A. H. *J. Am. Chem. Soc.* 2011, 133 (51), 20754–20757. (c) Townsend, E. M.; Schrock, R. R.; Hoveyda, A. H. *J. Am. Chem. Soc.* 2012, 134 (28), 11334–11337. (d) Wang, C.; Yu, M.; Kyle, A. F.; Jakubec, P.; Dixon, D. J.; Schrock, R. R.; Hoveyda, A. H. *Chem. – A Eur. J.* 2013, 19 (8), 2726–2740. (e) Wang, C.; Haeffner, F.; Schrock, R. R.; Hoveyda, A. H. *Angew. Chemie Int. Ed.* 2013, 52 (7), 1939–1943.
- (72) Endo, K.; Grubbs, R. H. *J. Am. Chem. Soc.* **2011**, 133 (22), 8525–8527.
- (73) Keitz, B. K.; Endo, K.; Herbert, M. B.; Grubbs, R. H. *J. Am. Chem. Soc.* **2011**, 133 (25), 9686–9688.
- (74) Keitz, B. K.; Endo, K.; Patel, P. R.; Herbert, M. B.; Grubbs, R. H. *J. Am. Chem. Soc.* **2012**, 134 (1), 693–699.
- (75) Rosebrugh, L. E.; Herbert, M. B.; Marx, V. M.; Keitz, B. K.; Grubbs, R. H. *J. Am. Chem. Soc.* **2013**, 135 (4), 1276–1279.

- (76) Hartung, J.; Grubbs, R. H. *J. Am. Chem. Soc.* **2013**, *135* (28), 10183–10185.
- (77) Quigley, B. L.; Grubbs, R. H. *Chem. Sci.* **2014**, *5* (2), 501–506.
- (78) Bronner, S. M.; Herbert, M. B.; Patel, P. R.; Marx, V. M.; Grubbs, R. H. *Chem. Sci.* **2014**, *5* (10), 4091–4098.
- (79) Dornan, P. K.; Wickens, Z. K.; Grubbs, R. H. *Angew. Chemie Int. Ed.* **2015**, *54* (24), 7134–7138.
- (80) Herbert, M. B.; Suslick, B. A.; Liu, P.; Zou, L.; Dornan, P. K.; Houk, K. N.; Grubbs, R. H. *Organometallics* **2015**, *34* (12), 2858–2869.
- (81) Liu, P.; Xu, X.; Dong, X.; Keitz, B. K.; Herbert, M. B.; Grubbs, R. H.; Houk, K. N. *J. Am. Chem. Soc.* **2012**, *134* (3), 1464–1467.
- (82) Sanford, M. S.; Love, J. A.; Grubbs, R. H. *J. Am. Chem. Soc.* **2001**, *123*, 6543.
- (83) Vorfalt, T.; Wannowius, K.-J.; Plenio, H. *Angew. Chemie* **2010**, *122* (32), 5665–5668.
- (84) Vorfalt, T.; Wannowius, K.-J.; Plenio, H. *Angew. Chemie* **2010**, *122* (32), 5665–5668.
- (85) Ashworth, I. W.; Hillier, I. H.; Nelson, D. J.; Percy, J. M.; Vincent, M. A. *Chem. Commun.* **2011**, *47* (19), 5428–5430.
- (86) Thiel, V.; Hendann, M.; Wannowius, K.-J.; Plenio, H. *J. Am. Chem. Soc.* **2012**, *134* (2), 1104–1114.
- (87) Nuñez-Zarur, F.; Solans-Monfort, X.; Rodríguez-Santiago, L.; Sodupe, M. *Organometallics* **2012**, *31* (11), 4203–4215.
- (88) Ashworth, I. W.; Hillier, I. H.; Nelson, D. J.; Percy, J. M.; Vincent, M. A. *ACS Catal.* **2013**, *3* (9), 1929–1939.
- (89) Keitz, B. K.; Endo, K.; Patel, P. R.; Herbert, M. B.; Grubbs, R. H. *J. Am. Chem. Soc.* **2012**, *134* (1), 693–699.

(90) (a) Dang, Y.; Wang, Z.-X.; Wang, X. *Organometallics* **2012**, *31* (20), 7222–7234. (b)
Dang, Y.; Wang, Z.-X.; Wang, X. *Organometallics* **2012**, *31* (24), 8654–8657.